

**Detailed Joint Structure in a Geothermal Reservoir  
from Studies of Induced Microearthquake Clusters**

W. Scott Phillips

MS C335, Los Alamos National Laboratory, Los Alamos, NM 87545  
wsp@lanl.gov  
(505) 667-8106

Leigh S. House

MS D443, Los Alamos National Laboratory, Los Alamos, NM 87545  
house@seismo5.lanl.gov  
(505) 667-1912

Michael C. Fehler

MS D443, Los Alamos National Laboratory, Los Alamos, NM 87545  
fehler@seismo5.lanl.gov  
(505) 667-1925

All authors at:

Division of Earth and Environmental Sciences,  
Los Alamos National Laboratory, Los Alamos, New Mexico  
LAUR 94-3846

## Abstract

Microearthquake clusters form distinct, planar patterns within five study regions of a geothermal reservoir undergoing hydraulic fracturing at Fenton Hill, New Mexico. The patterns define individual, slipping joint surfaces of dimension 40 to 120 m, containing 80 to 150 events each. Sharp, straight edges truncate the clusters; we interpret these as marking intersections with aseismic joints. Each edge orientation is consistent with an intersection between the active joint and a plane orientated parallel to one of the other clusters we identify. Therefore, it appears that cluster shapes constrain the geometry of seismic and aseismic joints; both could be important components of the fluid-flow network. The distribution of inferred slip plane orientations is consistent with, but fails to provide sufficient constraint to differentiate conclusively between two, very different, stress field estimates, one measured using pressurization and wellbore breakouts, the other using focal mechanisms of the largest microearthquakes. An impermeable joint model, requiring pore pressure in excess of the normal stress on a joint before slip can occur, was inconsistent with many of the inferred slip plane orientations.

The high-quality locations were possible because events from the same cluster generated nearly similar waveforms, permitting the precise determination of relative arrival times. Standard deviations of arrival-time residuals fall between 0.1 and 1.1 ms for these clusters. Major axes and aspect ratios of the 90% confidence ellipsoids range from 6 to 28 m and 1.5 to 8, respectively. Small events dominate the seismic energy release and thoroughly populate the identified, active joints, allowing the hypocenters to reflect details of the joint structure.

To further investigate the reservoir structure, we applied a source-array, slant-stack technique to waveforms from the well-located clusters, yielding directions that scattered energy left each cluster. By studying paths of scattered waves, we expected to pinpoint impedance contrasts that might have indicated concentrations of fluid-filled joints. However, results show that scattered energy in the S-wave coda left the source region in the same direction as the direct S wave. Direct waves may have excited borehole tube waves that became trapped in the vicinity of the geophone tool, overwhelming any energy scattered from the reservoir.

## Introduction

Induced microearthquake data collected from a geothermal reservoir at Fenton Hill, New Mexico, provide an opportunity to study relationships between seismicity and high-pressure fluids in a volume of crystalline rock at depths of 3 to 4 km. The reservoir was created by hydraulic fracturing which opened fluid paths that were to be used to extract heat from the rock. In one of the earlier successful applications of microseismic techniques to such man-made or hot-dry-rock reservoirs, a hydraulic connection to the pressurized well was achieved by drilling into the zone that was seismically active during fracturing. House (1987) presents the hypocentral results used to determine the drilling target. Because of the requirement that seismically active areas must be hydraulically connected to the pressurized well, the successful connection is consistent with the usual model of shear-slip seismicity induced by an increase in pore pressure along joints or planes of weakness in the rock.

Only gross features of the 1 km by 1 km by 300 m cloud of seismicity were considered in obtaining the hydraulic connection at Fenton Hill. Since then, statistical and clustering studies have shown that structures exist within the large cloud of seismicity (Fehler et al., 1987; Fehler, 1989; Roff et al., 1996). If we can obtain detailed maps of the seismicity, perhaps we will be able to reconstruct the joint network that provides fluid-flow or high-pressure paths through the rock mass. Unfortunately, microseismic patterns can not be relied on to outline joint patterns completely. In particular, slip may occur on joints that are oriented closest to failure with respect to the stress field, but may not occur on others. Thus, some interpretative insights will be necessary to infer joint-network flow models from seismicity. If successful, we anticipate testing flow models against pressurization and tracer data that have been collected at Fenton Hill. Results from the well-constrained experiment at Fenton Hill may help to interpret seismicity in other situations in which high-pressure fluids are, or may be important, such as oil and gas reservoirs (e.g. Warpinski et al., 1996; Keck and Withers, 1994; Phillips et al., 1996), fault zones (Johnson and McEvilly, 1994; 1995) and volcanic environments (e.g. Fremont and Malone, 1987).

The first step in this process is to obtain high-resolution hypocentral locations of induced microearthquakes at Fenton Hill. Here, we demonstrate this is possible by analyzing spatial clusters that are composed of large numbers of microearthquakes that have generated similar waveforms.

The spatial clustering of earthquakes offers insights into the

deformation of the earth on many scales. Clustered events often produce similar seismograms (Omori, 1905), the result of a common source mechanism as well as common path and site effects. Such earthquakes are termed “similar,” “doublet” or “multiplet” events. Geller and Mueller (1980) suggested that similar, central California earthquakes resulted from slip on the same fault-zone asperity. Local- and regional-scale clusters, many containing similar events, have been identified in Japan (Motoya and Abe, 1985; Ito 1985, 1990), the Virgin Islands (Frankel, 1982), Mt. St. Helens (Fremont and Malone, 1987), Nevada (Stauder and Ryall, 1967), Washington (Johnson and Zollweg, 1987a, b; Johnson, 1989), Utah (Pechmann and Thorbjarnardottir, 1990) and California (Ishida and Kanamori, 1978; Pechmann and Kanamori, 1982; Poupinet et al., 1984).

Recent field studies exploiting high-quality site effects, including the use of borehole seismometers, have shown that similar-microearthquake clustering is common in fault-zone regions. Aster and Scott (1993) used a single-link, waveform cross-correlation method to assign 27% of their Anza, California events to clusters when the similarity criterion was chosen to maximize the number of clusters. Nadeau et al. (1994, 1995) used similar methods and obtained precise, relative locations of clustered events recorded by the high-resolution, borehole-sited seismographic network at Parkfield, California. Over half of their events fell into similar-event clusters.

In this study, we selected microearthquakes from five regions of the Fenton Hill reservoir in which spatial clustering is apparent, without regard to waveform similarity. We chose to sample a range of depths and concentrations of seismic activity. Similar, but not identical, waveforms predominate within each cluster. We will describe data processing and location techniques that resulted in patterns that define individual, seismically active joints and allowed us to infer positions of aseismic joints at Fenton Hill.

Using the high-precision relative locations, we studied scattered waveforms using array techniques (Spudich and Bostwick, 1987) in an attempt to further image the pressurized joint system. However, we found backscattered energy difficult to observe because of strong, near-station, multiple scattering, a surprising result given the highly favorable site conditions expected for downhole recording.

## Data

In December 1983, Los Alamos National Laboratory carried out the Massive Hydraulic Fracturing (MHF) experiment at the Hot Dry Rock

geothermal site at Fenton Hill, New Mexico. Over 21,000 m<sup>3</sup> of water were injected in 61 hours at a wellhead pressure of 48 MPa. The injection point was 3460 m deep in predominantly granitic, Precambrian basement under the southwest flank of the Jemez caldera. The purpose of the hydraulic fracturing was to create a reservoir through which fluids could be circulated to extract heat. Dreesen and Nicholson (1985) and Franke and Nunz (1985) give operational details of the fracturing experiment.

The MHF experiment was instrumented with borehole sensors to monitor any accompanying seismic activity (House, 1987; Figure 1). Two vertical-component sensors were sited near the top of the basement (GT-1, PC-1) at depths greater than 500 m. Two pressure- and temperature-hardened, triaxial, sensors were sited within the basement at depths of 2855 m (EE-1) and 3300 m (EE-3). Data were recorded continuously on analog tape and later digitized at 5000 Hz. Event detection yielded over 11,000 locatable microearthquakes.

Shear slip predominates in Fenton Hill seismicity (Pearson, 1981; Albright and Pearson, 1982; House and Jensen, 1987); however, a few low-amplitude, tensile events were observed early in the MHF experiment (Bame and Fehler, 1986). Moments of the induced seismic events range between  $10^{13}$  and  $10^{18}$  dyne-cm, with corner frequencies between 60 and 600 Hz, yielding estimates of source radii of 3 to 30 m and an average stress drop of 3.7 bar (Fehler and Phillips, 1991). The cumulative-moment  $\beta$ -value was 1.5 to 1.9, higher than the  $\beta$ -value of 0.67 that is commonly observed in fault zones (Molnar, 1979), indicating a high proportion of small events. The  $\beta$ -value is the analog to the  $b$ -value, using moment in place of magnitude. We use the  $\beta$ -value because we have not calibrated a magnitude scale for Fenton Hill events.

Of the locatable microearthquakes, over 8000 yield high-quality locations (RMS arrival time residual < 3 ms) using a constant velocity model ( $v_p=5.92$ ,  $v_s=3.5$ ) and station corrections from downhole shots (Figures 2a, b). Seismicity fills a tabular volume, 1 km by 1 km by 300 m in size, striking N10°W and dipping 65° to the east. The diffuse nature of the seismicity indicates a volume of fractured material rather than a single, planar fracture (House, 1987). Fehler et al. (1987) and Fehler (1989, 1990) found large, planar features in Fenton Hill data sets, including the MHF experiment, using the three-point method. Roff et al. (1996) found over 70 planar- and linear-shaped clusters that aligned with the three-point results by clustering events based on their S-to-P amplitude ratios. Microearthquake clustering is evident in the depth view looking west in Figures 2a and 2b. Selection boxes for the five clusters we analyze in greater detail are indicated in Figure 2b. Vertical component EE-1

seismograms from six events, three from each of clusters 1 and 2 are shown in Figure 3. Waveforms are quite similar within clusters, but very different between clusters.

Because the microearthquake waveforms were recorded and played back using analog tape decks, variations in the tape speed and in the positions of the tape heads could affect timing. To eliminate the tape-speed effect, we oversampled the 1 KHz, IRIG-B time codes using Fourier techniques to obtain time corrections at 100 ms intervals throughout the data. We found the time corrections to fluctuate sinusoidally with periods of roughly 2 s and maximum deviations normally less than a sample interval (0.2 ms). The correction was ignored in such cases. For a few records, the corrections were larger than a sample interval and these arrival times were thrown out. Our other problem was that the analog tape decks employed two, adjacent tape heads. The timing offset introduced by the tape heads was as large as 10 ms and changed occasionally when the tape heads slipped. On one tape (containing three-component data from geophones in wells EE-1 and EE-3) we cross-correlated high- and low-gain EE-1 signals that had been written by different tape heads to correct for tape-head offset. On the second tape (containing vertical-component data from geophones in wells EE-1, GT-1 and PC-1), EE-1 data and the time code were written by different tape heads, so the tape-head offset could be obtained by cross-correlating the EE-1 signal with that of the first tape. These corrections were of sample-interval precision.

## Methods

We applied two techniques to study the reservoir produced by the hydraulic fracturing. First, spatial clusters of events were taken from the data set and re-analyzed to obtain precise, relative locations. Then a slant stack was applied using the cluster locations as a source array to study the scattered wavefield.

*Precise relocation of similar-event clusters.* To measure relative arrival times precisely, we grouped microearthquakes spatially (Figure 2), obtaining many similar-waveform events in the process. Seismograms from cluster 2 (Figure 3) illustrate the advantage of analyzing clustered events at one time. Shear waves from cluster 2 are emergent, which make it difficult to determine arrival times consistently during routine processing, when many events of different character are interspersed. When we processed cluster events together it became easier to choose the same point in the waveform signature each time.

To determine arrival times from cluster events, we chose a prominent peak of the waveform rather than the first break. Peaks can be determined with lower error than first arrivals when the signal to noise is low. Arrival times were chosen manually. We tested waveform cross-correlation, arrival-time techniques on data from cluster 1, but the resulting corrections were so small that changes in the location pattern were barely perceptible.

We used two methods to calculate relative locations of cluster events. A master event method (Everndon, 1969) was based on station corrections obtained by fixing the location of one, well-recorded event. A joint-hypocenter determination (JHD; Douglas, 1967; Freedman, 1967; Dewey, 1972) was performed by fixing the cluster centroid to that of the original cluster locations. This position was a good estimate of the actual centroid, based on velocities (5.92 and 3.5 km/s for P and S waves, respectively) and station corrections from downhole shots. After adjusting the master-event centroid, the two methods gave nearly identical results.

Following Flinn (1965), we obtained 90% joint marginal confidence regions from the JHD calculation, using the arrival-time residual variance for the entire cluster as an estimate of the data variance (Table 1). Highly eccentric errors can stretch point- or linear-shaped clusters into linear- or planar-shaped clusters. To determine the significance of a cluster pattern we compare the shape, orientation and size of the confidence ellipsoid to those of the cluster. For example, when confidence ellipsoids are linear (major axis much greater than the intermediate and minor axes) we compare orientations of the major axis with the cluster pattern. When ellipsoids are planar (major and intermediate axes much greater than the minor axis) we compare orientations of the minor axis with the normal to the plane of the cluster.

*Slant stacking cluster data.* Following Spudich and Bostwick (1987), we used a cluster of similar microearthquakes as a source array to study the scattered wavefield. Because clusters contained similar microearthquakes, thus similar focal mechanisms, we were confident that wavelets would stack constructively when aligned according to their correct velocity and propagation direction.

Before stacking, we threw out any multiple-event data to eliminate secondary-event contamination of the coda. We then applied the slant-stack technique as follows: 1) a reference event was chosen, along with a time interval over which to carry out the stacking, 2) for a given plane-wave propagation direction and an estimate of the source-region velocity, delay times relative to the reference event were calculated for all cluster

events, 3) records were shifted by their delay times, normalized by their RMS signal, and stacked, and 4) RMS amplitude was calculated for the stack over the given time interval. Data were stacked over adjacent, non-overlapping 10 ms windows starting with the S wave. We then plotted RMS-stack amplitude for a fixed velocity on two equal-area stereograms, one for energy leaving the cluster in the upward direction, the other downward. For a contrasting view, we also stacked the entire seismogram, using a fixed direction and velocity.

It is common practice to low-pass filter seismograms before stacking to eliminate spatial aliasing (Spudich and Bostwick, 1987). Equating a location error of 10 m to a quarter wavelength, we obtain a low-pass corner of roughly 100 Hz (using the S-wave velocity of 3.5 km/s). Working with Fenton Hill data, we found that filtering caused no significant change in the results. We applied a nominal, 200 Hz, low-pass filter to obtain the results shown here.

We considered a single velocity in the slant stack. Because we restricted analysis to the S-wave coda, the velocity was set to 3.5 km/s, an average S-wave velocity throughout the reservoir, determined from shot data. The injection of water may have affected the velocity (Block et al., 1994) but the stack patterns were not sensitive to changes in stacking velocity. However, we were able to find a velocity which maximized the slant-stack energy. This velocity was roughly the P-wave velocity for direct P-wave and P-coda windows, and dropped to the S-wave velocity for direct S-wave and S-coda windows (Figure 4), supporting our use of S-wave velocities to study the S coda. Of course, these maximum-stack velocities depended on the velocities used to obtain the locations. Under restrictive assumptions, we can estimate the P-to-S velocity ratio from analyses of this sort (Phillips et al., 1992).

## Results

*Relocation of event clusters.* We extracted five clusters of microearthquakes from the Fenton Hill data set using boxes of unlimited east-west extent (Figure 2b). To avoid introducing artifacts, the boxes were not allowed to cross the main concentration of events within each cluster. After redetermining arrival times and hypocenters, residual variances decreased 35% to 80%, depending on the cluster (calculated from Table 1). To summarize location errors, we fit a set of orthogonal axes to the distribution of 90% confidence ellipsoid axes using an L1-norm scheme (Table 2). Major axes often trend in an east-west direction for this distribution of stations. The small misfits (at most  $20^\circ$ ) indicate consistently oriented ellipsoids. The tabulated axes magnitudes are median



values for each cluster (Table 2). Major axes range from 6 to 28 m, minor from 0.8 to 13 m, depending on the cluster. Aspect ratios (ratio of ellipsoid major and minor axis lengths) are between 1.5 and 8.

To illustrate the effect of repicking the data, we show initial and relocated hypocenters of cluster 1 in Figures 5a and b, respectively. The hypocenter pattern tightens dramatically after relocation, falling onto a nearly vertical plane of dimension 40 m, striking N30°W. In face-on view, sharp, straight edges bound the location pattern, roughly forming a parallelogram. This cluster is isolated from the rest of the seismicity (Figure 2b), eliminating any chance that the observed edges are an artifact of the event-selection box. The best-fit 90% confidence ellipsoid is elongated with an aspect ratio of 7.5. The major axis measures 6 m, trends N75°W and plunges 39° (Table 2). Since the major axis of the elongated confidence ellipsoid is oblique to the cluster, we consider the cluster orientation and shape to be significant.

Relocation results for cluster 2 (Figure 5c) are similar to those of cluster 1. The hypocenters fall onto a vertical plane of dimension 100 m, striking N40°W. The face-on view shows a filled parallelogram pattern similar to cluster 1, with some edges better defined than others. A set of events that generated significantly different S waveforms lines up near one of the edges. Because arrival times for these waveforms were determined differently, this set of events may be less well located relative to the main cluster than relative to each other. Thus, the orientation of this sub-cluster may be significant, but its position within the main cluster is less so. The confidence ellipsoids are not extremely eccentric but are somewhat planar for cluster 2 (similar major and intermediate axes, both twice the minor axis), dipping steeply and striking roughly N70°W (the minor axis trends N20°E). This is 30° from the strike of the cluster plane.

Cluster-3 event relocations are scattered (Figure 5d), although a number of events fall into a line of length 25 m, trending roughly east-west with very little plunge from the horizontal. This pattern aligns within 15° or so with the azimuth of the highly elongated confidence ellipse (aspect ratio 8, major axis 16 m) and, conservatively, will be considered a location error artifact.

Cluster 4 contains two parallel, planar distributions, striking N45°E and dipping 45° to the northwest (Figure 5e). The two planes are separated by 50 m in the vertical direction. The longest dimension of the upper distribution measures 100 m. Straight bounding edges can be seen in the map view. Confidence ellipsoids are not particularly eccentric (aspect ratio of 3), with a major axis 28 m long that trends to the west and

plunges  $19^\circ$ .

Relocated hypocenters of Cluster 5 fall into a number of sub-clusters (Figure 5f). Two elongated patterns are easily visible, both trending  $N20^\circ W$ , the largest of dimension 130 m (Cluster 5A). Additional events give the cluster-5 location plots a scattered appearance. To isolate possible patterns, we grouped events by P-wave polarity at station PC-1. Events from cluster 5A have positive polarities and were easily separated from the main group (Figure 5g). The most populous, negative-polarity cluster (5B) is planar, striking  $N20^\circ E$ , dipping  $45^\circ$  to the east, and is located above cluster 5A (Figure 5h). As for the previous planar clusters, sharp, straight edges also bound clusters 5A and 5B. Confidence ellipsoids are similar for 5A and 5B and are not eccentric (aspect ratios less than 2), with major axes just over 20 m in length.

*Source-array slant stack of the S coda.* To obtain directions that seismic energy left each cluster, we applied a slant stack to seismograms from station EE-1. Vertical-component results will be presented here; horizontal-component results are similar.

Sample results are shown in Figure 6 where we contour the RMS slant-stack signal versus propagation direction leaving the cluster, for S- and coda-wave time windows, and for clusters 1 and 5B. The coda and S-wave results match closely for cluster 1, with stack maxima close to the straight-ray, direct-wave propagation direction. Coda and direct-wave results also match for cluster 5B, but the maxima indicate propagation directions oriented roughly  $25^\circ$  from the straight-ray direction. In addition, cluster 5B results indicate secondary peaks over a wide range of propagation directions. However, these directions do not indicate that scattering from the fractured reservoir is any higher than from surrounding areas. We find no evidence of preferential scattering from the reservoir in any of the cluster results.

We stacked longer time windows of cluster 1 data for two directions: towards and away from geophone EE-1 (Figure 7). In the higher energy, towards-EE-1 stack, periodic amplitude fluctuations occurred in the coda at roughly 60 ms intervals. As seen earlier (Figure 6), the coda contained little backscattered energy that initially propagated away from the geophone.

To summarize results, we show the maximum-RMS stack for all propagation directions versus time for each cluster in Figure 8. We also show the maximum-RMS values falling within  $15^\circ$  of the straight-ray direction between cluster and station. For all but cluster 5B, the maximum

and straight-ray direction stacks are nearly the same.

## Discussion

After relocation, nearly all microearthquakes from five Fenton Hill study regions fall into distinct planar clusters. The only exception is cluster 3, for which seismicity is scattered except for a central feature whose shape may be affected by highly eccentric errors. The planar clusters contain between 80 and 150 events, are isolated from other seismicity and are bounded by straight, often parallel edges.

In statistical studies, Fehler and Phillips (1991) showed that smaller events released a majority of the seismic energy at Fenton Hill (cumulative-moment  $\beta$  value 1.5 to 1.9, moments  $10^{13}$  to  $10^{18}$  dyne-cm). This is opposite to what has been observed in fault zones where larger events dominate the energy release ( $\beta=0.67$ ; Molnar, 1979) but is similar to what is often observed in seismic swarms and volcanic sequences (Sykes, 1970). The high  $\beta$  value at Fenton Hill is consistent with high, small-scale heterogeneity in permeability and pore pressure along the joint surfaces that only allow slip to progress small distances, as was suggested by Sykes (1970) for swarms. Because energy was released in many small ruptures rather than fewer large ones, location patterns more clearly reflect the orientation and extent of slipping joints.

*Cluster edges and aseismic joints.* To summarize our cluster-relocation results, we plotted orientations of normals and edges of planar clusters in stereo projection (Figure 9). Orientations were measured from Figures 5b-h which have been aligned by eye along the strike or trend of the event distribution. The true edge vectors (open circles, Figure 9) were calculated from the measured edge vectors (parallel to a projection plane) by taking the cross product with the normal to the projection plane and then with the normal to the event plane (thus crossing normals to two non-parallel planes that both contain the true edge vector). To simplify the plot, when two symbols representing sub-parallel edge vectors from the same cluster overlapped, one was removed. The planar clusters can be separated into three types based on their orientations: 1) three planes strike to the northwest and dip steeply (clusters 1, 2 and 5A), 2) one plane strikes northeast with shallow dip to the northwest (cluster 4), and 3) one plane strikes north-northeast with shallow dip to the east (cluster 5B). Edges can also be placed in groups, falling roughly parallel to intersections of the observed planar orientations. Edges of planes 1, 2, 4, and 5A are parallel to intersections of the steeply dipping planes (type 1) with plane 4 (type 2). Edges of planes 1, 2, 5A and 5B are parallel to intersections of the steeply dipping planes (type 1) with plane 5B (type 3). Edges of planes

4 and 5B are parallel to the intersection of these two planes with each other (types 2 and 3). This accounts for all edge vectors and plane-type pairs. These results give us additional confidence in our interpretation that straight edges mark intersections with other joints. The coincidence between edge vectors and planar intersections is remarkable because the clusters represent only a small sample (roughly 10% of the well-located events) of the seismicity induced by the hydraulic fracturing. Of course, a cluster edge does not fully constrain the position of a cross-cutting aseismic joint, but if we can guess a range of orientations based on these results, we may be able to reconstruct more than the seismically active portion of the joint network.

As discussed above, the steeply dipping clusters have well-defined edges that could result from truncation by aseismic joints oriented parallel to cluster 4, yet cluster 4 has an edge that could result from truncation by an aseismic joint oriented parallel to the steeply dipping clusters. Thus, similarly oriented joints can be seismic or aseismic, depending on their position within the reservoir. This may indicate a spatially heterogeneous stress field, possibly varying with time during the fluid injection (Cornet and Julien, 1989; Scotti and Cornet, 1994). Furthermore, the seismic response of two intersecting joints may depend on which joint is pressurized first.

We are encouraged that precise relocations can help us identify and partially constrain the positions of aseismic joints in the reservoir. However, it is commonly held that seismically active joints should be more important fluid or fluid pressure conduits than inactive joints because of the increased permeability associated with the displacement of rough surfaces (Brown, 1987). From *in-situ* measurements in Cajon Pass, Long Valley and Yucca Mountain boreholes under hydrostatic conditions, Barton et al. (1995) showed that flow occurs preferentially along joints or fractures oriented best for shear failure. However, if Fenton Hill microearthquakes are induced by increases in pore pressure along the joint, the spatial isolation of the clusters requires pressure connection through an aseismic joint. In addition, Cornet and Yin (1995) showed that the most hydraulically significant zone was aseismic during pressurization at the Le Mayet de Montagne site in France. Because focal mechanisms were not parallel to a flowing fracture, Scotti and Cornet (1994) proposed that seismicity occurred along fractures of multiple orientations where they intersected the hydraulically conductive, but aseismic, main fracture. Therefore, we cannot ignore the role that aseismic joints might play in the behavior of pressurized fluids. In fact, the opening of joints perpendicular to the minimum principal stress, nearly an aseismic process (Bame and Fehler, 1986), is often invoked to explain the overall shape and orientation

of the Fenton Hill reservoir seismicity.

*Comparison with previous Fenton Hill results.* Earlier work that identified location patterns in Fenton Hill seismicity is consistent with our cluster-orientation observations. Planar features obtained using the three-point method (Fehler et al., 1987; Fehler, 1989) and planar and linear features obtained using a clustering technique based on S-to-P amplitude ratios (Roff et al; 1996) are plotted along with our cluster results in Figure 10. Normals to planes (squares) concentrate around northeast and southwest directions, while linear features (circles) trend northwest-southeast and plunge from vertical to horizontal. In addition, although less common, shallow dipping planes with normals in the southeast quadrant, similar to cluster 4, have been observed. We find cluster 5B on the edge of the large distribution of planar normals pointing in southwesterly directions. We expected some uncertainties in the earlier two studies because only routinely determined event locations were available for calculating orientations. The three-point planes are large, extending a sizable fraction of the reservoir and location error should not affect orientations very much. However, because of their smaller size, orientations of S-to-P clusters may contain larger error, but general agreement with orientations of the precisely located clusters help confirm the S-to-P cluster results.

*Stress Fields.* To understand fluid flow through a network of joints, we must know what the stress field is. Assuming that slip occurs in some direction parallel to the seismically defined planes and that the stress field is homogeneous, we searched for the stress field that is most consistent with the slip-plane orientations using a Coulomb slip condition with cohesive strength set to zero. To do this, we performed a grid search over orientations of the principal stress axes, ratios of maximum-to-minimum and intermediate-to-minimum principal stresses and pore pressure. We constrained vertical stress to be lithostatic (95 MPa at injection depths) and the minimum stress to be the pressure needed to hold fractures open (about 45 MPa, D. Brown, personal communication, 1996). In addition, stress fields that caused fracture along any plane (shear to effective normal stress ratio greater than 1.0) at natural hydrostatic pressure (28 MPa) were eliminated from consideration. Because Fenton Hill seismicity was only associated with fracturing operations, we also tried to minimize the number of seismically defined planes that slipped (the above stress ratio greater than 0.6) under in-situ conditions. Finally, because we have ten times as many S-to-P amplitude cluster planes, we weighted three-point and relocation cluster planes by 10. Following this, we test two Fenton Hill stress fields, one estimated using pressurization and borehole breakout data, the other with focal mechanism data, for consistency with

the seismically defined slip planes.

Pore pressure had the largest effect in this exercise. If pore pressure was set to the highest estimate of downhole pressure during fracturing ( $>70$  MPa), nearly any stress field satisfying our constraints also satisfied the planar orientations. This was also true for pore pressures of 60 MPa. We evaluated stress fields using an intermediate pore pressure value of 40 MPa. This seems more reasonable than using the maximum pore pressure because we expect pore pressure to decrease to *in-situ* levels with distance from the injection point (Cornet and Yin, 1995). At 40 MPa pore pressure, we obtained a near-vertical maximum principal stress that is consistent with slip on 95% of the seismically active planes while allowing less than 10% of them to slip under *in-situ* conditions (Figure 11, top). However, this stress field predicts overall extension of the seismicity in the east-west direction, if extension is controlled by the opening of joints perpendicular to the minimum, principal-stress axis. The best-fitting stress field with minimum principal axis perpendicular to the overall seismicity is consistent with 80% of the slip planes while still allowing less than 10% to be active under *in-situ* conditions.

A stress field measured using pressurization and borehole breakout data is detailed by Fehler (1989) and is used by reservoir engineers in their work at Fenton Hill. This stress field has maximum principal stress vertical, minimum principal stress trending N104°E, maximum-to-minimum stress ratio of 2 and intermediate-to-minimum stress ratio of 1.5. We found appropriate values for the principal stresses given the lithostatic and fracture-opening pressure constraints outlined above. Setting pore pressure to 40 MPa, this stress field is consistent with 75% of the seismically active slip planes (Figure 11, middle), but allows 20% of the planes to slip under *in-situ* conditions. Rotating this stress field 30° CCW about the maximum principal stress axis (vertical) would yield a stress field that would align better with the planar orientations and also be more consistent with the north-south extension of the overall seismicity. Because a field-deployment oversight resulted in systematic error of unknown magnitude in downhole tool orientation used to study wellbore breakouts (K. Burns, personal communication, 1989), this rotated stress field may be reasonable. In any case, some of the shallow dipping planes with normals in the southeast quadrant will be hard to satisfy with this stress field, rotated or not.

The stress field derived by inverting focal mechanisms from a set of 187 of the largest events that were well recorded by an array of surface seismic stations, gave a maximum principal stress that is nearly horizontal and aligned parallel to the strike of the overall seismicity. The minimum

principal stress axis plunges  $60^\circ$  in an easterly direction. Unfortunately, we can not satisfy the lithostatic and minimum stress constraints using this stress field without a maximum-to-minimum stress ratio greater than 4. Such stress fields would easily produce seismic activity under *in-situ* conditions, which is not observed. Instead, we chose to rotate this stress field about the maximum principal axis by  $30^\circ$  (CCW, looking along the axis) to bring the minimum principal axis perpendicular to the overall seismicity and to more easily fit the lithostatic and minimum principal stress constraints. For a pore pressure of 40 MPa we found that 80% of the planes are consistent with this stress field (Figure 11, bottom), but 60% of the planes slip under *in-situ* conditions. Some shallow dipping planes with normals in the southeast quadrant are inconsistent with this stress field. It has been demonstrated that injection-induced stress changes make it difficult to measure regional stresses using focal mechanisms of induced microearthquakes (Cornet and Julien, 1989; Scott and Cornet, 1994; Cornet and Yin, 1995). However, this means focal mechanisms can be used to study stress changes during injection. Resolving the differences between focal mechanisms and other stress measurements, including the seismically active joint orientations may lead to greater understanding of fluid flow and pressure patterns during injection.

*Impermeable joints.* To this point, we have assumed microseismic events result from slip along joints of elevated pore pressure under a Coulomb-type failure law, which requires that joints be permeable. However, the low leak-off rates observed in pressure tests (D. Brown, personal communication, 1996) indicate that Fenton Hill joints may be no more permeable than the rock matrix and that it may be difficult to raise pore pressure inside a joint without hydraulically opening it first. To test this idea, we performed the stress-field grid search while allowing slip on any plane for which pore pressure is greater than the normal stress (again, ignoring cohesive strength). Results gave maximum principal stresses near vertical. For a pore pressure of 50 MPa, only 56% of the seismically active planes could be opened and allowed to slip. Clearly, the impermeable joint model is less consistent with the observed slip planes than the permeable joint model.

*Automatic clustering methods.* In this study, we analyzed only 10% of the seismic events available for a single fracturing experiment (MHF) at Fenton Hill. To obtain the high-precision locations, we determined arrival times manually, a slow and tedious process. It will be important to develop automatic methods to identify clusters and determine arrival times if we wish to analyze data sets of 10,000 or more events in a reasonable amount of time. Clustering Fenton Hill events by S-to-P amplitude ratio and proximity discards too many cluster events (Roff et al.,

1996). Clustering by waveform similarity via cross-correlation (Aster and Scott, 1993), including simultaneous arrival-time determination using the matrix of relative time delays, was the obvious next step; however, a straightforward implementation fared poorly with Fenton Hill data (A. Roff, personal communication). Along with occasionally low signal-to-noise and instrument saturation, problems included a non-negligible variety of waveforms within spatial clusters that resulted in cycle skipping, especially for near-nodal P-wave phases. The variation in waveforms may result from a near-source path effect when events are more than a wavelength apart (30 m for a 200 Hz compressional wave), or from variations in source orientation, especially slip direction, because of stress changes caused by prior slip on the joint (e.g. Cornet and Yin, 1995). After applying the cross-correlation procedure, clusters 1-5 described in this study were broken into smaller, unrecognizable groups, many events being discarded in the process. We conclude that more complex methods are necessary for algorithms to process the data as effectively as the human eye. Manually-determined results should be used as a guide.

*Secondary arrivals from source-array, slant-stack studies.* We applied array techniques to the S coda of cluster microearthquakes to map scattering features within the hydraulically-fractured rock mass in the hope of identifying fluid-filled zones. For four of five clusters, scattered waves left in the direction of the station. Cluster 5B was the exception, yet S- and coda-wave directions were nearly the same. This cluster occurred late in the experiment and ray paths may have bent around the water-inflated reservoir. In all cases, the coda-wave energy left the source region in the same direction as the S wave. This implied that multiple scattering near the station dominated the coda. Spudich and Bostwick (1987) obtained similar results applying source-array techniques to data from surface stations. In our case, the sensor was sited in a deep, water-filled borehole, in which tube waves can be expected to propagate efficiently. The direct S wave may have excited a tube wave at the bottom of the borehole, at intersection points of fractures from earlier experiments, or at the bottom of the deepest casing. Once generated, some tube wave energy may have been trapped by the same features. For some clusters, we see pulses of scattered energy in the slant-stacked coda that may represent repeated passage of a reflected tube wave (Figures 7, 8).

## Conclusions

We studied microearthquake clustering and scattered wavefields in a data set of over 11,000 events collected using borehole seismometers, during hydraulic fracturing at a depth of 3460 m at Fenton Hill, NM. We selected clusters visually from a set of initial event locations. Taking



advantage of the similarity of cluster waveforms, we determined arrival times manually, choosing the same point in the waveforms each time.

For all but one cluster, nearly all relocated events fell into spatially distinct, planar patterns of 80 to 150 events. Fehler and Phillips (1991) showed that Fenton Hill seismicity had a higher-than-normal population of smaller events, consistent with a heterogeneous distribution of permeability and pore pressures along joints. Thus, the induced failure of a joint surface involved a large number of smaller events rather than a few larger events, causing pronounced clustering and allowing event locations to clearly delineate the slipping joint. Cluster patterns indicate orientations of joints along which sufficient resolved shear stress exists to cause slip. In addition, our results show that clusters are bounded by sharp edges that may result from a slipping joint being truncated by aseismic joints. Furthermore, the cluster-edge orientations are consistent with intersections of the active joint with joints oriented parallel to one of the other planar clusters we identified. Flow along aseismic joints may be important in the reservoir, and edges and linear features will help to constrain the positions and orientations of these possible fluid paths.

Orientations of inferred slip planes were used to evaluate two very different stress fields, one obtained using pressurization and wellbore breakout data, the other using focal mechanisms of large events recorded on a surface array. Both stress fields were reasonably consistent with the distribution of slip planes; however, because pore-pressure is not known well, we could not differentiate conclusively between them. In its favor, the pressurization-breakout stress field caused fewer observed planes to slip under in-situ conditions. We also evaluated an impermeable joint model of seismic slip, requiring pore pressure higher than normal stress before a joint can slip. Nearly half of the inferred slip planes were inconsistent with the best-fit stress field in this case.

In an attempt to identify waves scattered by the pressurized fracture system, we studied the scattered wavefield using the high-quality event hypocenters as an array of receivers (Spudich and Bostwick, 1987).. We found that scattered, S-coda energy left the source region in the same direction as the direct S wave. Thus, near-site multiple scattering dominates the scattered wavefield. The direct wave may have excited a tube wave at one or more borehole heterogeneities, with some energy remaining trapped in the vicinity of the geophone tool. Secondary scattering peaks are apparent in the stacks, but no preferential scattering from the reservoir fracture system is observed. Reservoir scattering may be difficult to observe with this method because new joints were being pressurized throughout the active time span of a given cluster (House and

Phillips, 1991).

## Acknowledgments

We thank Paul Johnson, Norma McFarland and Darrik Stafford for their roles in processing the microearthquake data set. Discussions with Bill Rodi, Yingping Li and Arthur Cheng were invaluable. Lee Steck and James Albright provided helpful comments on early drafts. We are grateful for reviews by Peggy Johnson and an anonymous referee that helped improve the manuscript. We also thank Hiroaki Niitsuma, Hiroshi Asanuma, Rob Jones and members of the MTC project for their encouragement and many technical discussions. This work was supported by the U. S. Department of Energy, Office of Basic Energy Sciences, Division of Geosciences and Engineering under contract W-7405-ENG-36.

## References

- Aki, K., M.C. Fehler, R. Aamodt, J.N. Albright, R. Potter and J. Tester, Interpretation of seismic data from hydraulic fracturing experiments at the Fenton Hill, New Mexico, Hot Dry Rock geothermal site, *J. Geophys. Res.*, **87**, 936-944, 1982.
- Albright, J. N., and C. F. Pearson, Acoustic emissions as a tool for hydraulic fracture location: Experience at the Fenton Hill Hot Dry Rock site, *J. Soc. Pet. Eng.*, **22**, 523-530, 1982.
- Aster, R. C., and J. Scott, Comprehensive characterization of waveform similarity in microearthquake data sets, *Bull. Seism. Soc. Am.*, **83**, 1307-1314, 1993.
- Bame, D. and M.C. Fehler, Observations of long-period earthquakes accompanying hydraulic fracturing, *Geoph. Res. Lett.*, **13**, 149-152, 1986.
- Barton, C.A., M.D. Zoback and D. Moos, Fluid flow along potentially active faults in crystalline rock, *Geology*, **23**, 683-686, 1995.
- Block, L. V., C. H. Cheng, M. C. Fehler, and W. S. Phillips, Seismic imaging using microearthquakes induced by hydraulic fracturing, *Geophysics*, **59**, 102-112, 1994.
- Brown, S.R., Fluid flow through rock joints: The effect of surface roughness, *J. Geophys. Res.*, **92**, 1337-1347, 1987.
- Cornet, F.H. and Ph. Julien, Stress determination from hydraulic test data and focal mechanisms of induced seismicity, *Int. J. Rock Mech. Min. Sci. & Geomech. Abstr.*, **30**, 789-795, 1989.
- Cornet, F.H. and J. Yin, Analysis of induced seismicity for stress field determination and pore pressure mapping, *PAGEOPH*, **145**, 677-700, 1995.
- Dewey, J.W., Seismicity and tectonics of western Venezuela, *Bull. Seism. Soc. Am.*, **62**, 1711-1751, 1972.
- Douglas, A., Joint epicentre determination, *Nature*, **215**, 47-48, 1967.
- Dreesen, D. S., and R. W. Nicholson, Well completion and operations for MHF of Fenton Hill well EE-2, *Trans. Geotherm. Res. Coun.*, **9**, Pt II, 105-

110, 1985.

Everndon, J.F., Identification of earthquakes and explosions by use of teleseismic data, *J. Geophys. Res.*, **74**, 3828-3856, 1969.

Fehler, M.C., Using dual-well seismic measurements to infer the mechanical properties of a Hot Dry Rock geothermal system, *J. Geophys. Res.*, **87**, 5485-5494, 1982.

Fehler, M. C., Stress control of seismicity patterns observed during hydraulic fracturing experiments at the Fenton Hill Hot Dry Rock geothermal energy site, New Mexico, *Int. J. Rock Mech. Min. Sci. & Geomech. Abstr.*, **26**, 211-219, 1989.

Fehler, M. C., Identifying the plane of slip for a fault plane solution from clustering of locations of nearby earthquakes, *Geophys. Res. Lett.*, **17**, 969-972, 1990.

Fehler, M. C., and D. Bame, Characteristics of microearthquakes accompanying hydraulic fracturing as determined from studies of spectra of seismic waveforms, *Trans. Geotherm. Res. Coun.*, **9, Pt II**, 11-16, 1985.

Fehler, M. C., L. S. House and H. Kaieda, Determining planes along which earthquakes occur: method and application to earthquakes accompanying hydraulic fracturing, *J. Geophys. Res.*, **92**, 9407-9414, 1987.

Fehler, M. C., and W. S. Phillips, Simultaneous inversion for Q and source parameters of microearthquakes accompanying hydraulic fracturing in granitic rock, *Bull. Seism. Soc. Am.*, **81**, 553-575, 1991.

Flinn, E.A., Confidence regions and error determinations for seismic event location, *Rev. Geophys.*, **3**, 157-185, 1965.

Franke, P. R., and G. J. Nunz, Recent developments in the hot dry rock geothermal energy program, *Geothermal Resources Council Annual Meeting, Preprints*, 1-4, 1985.

Frankel, A., Precursors to a magnitude 4.8 earthquake in the Virgin Islands: spatial clustering of small earthquakes, anomalous focal mechanisms and earthquake doublets, *Bull. Seism. Soc. Am.*, **72**, 1277-1294, 1982.

- Freedman, H.W., A statistical discussion of P residuals from explosions, Part II, *Bull. Seism. Soc. Am.*, **57**, 545-561, 1967.
- Fremont, M. and S. Malone, High precision relative locations of earthquakes at Mount St. Helens, Washington, *J. Geophys. Res.*, **92**, 10223-10236, 1987.
- Geller, R., and C. Mueller, Four similar earthquakes in central California, *Geophys. Res. Lett.*, **7**, 821-824, 1980.
- House, L. S., Locating microearthquakes induced by hydraulic fracturing in crystalline rock, *Geophys. Res. Lett.*, **14**, 919-921, 1987.
- House, L. S., and B. Jensen, Focal mechanisms of microearthquakes induced by hydraulic injection in crystalline rock, *EOS Trans.*, **68**, 1346, 1987.
- House, L.S. and W.S. Phillips, Imaging of a fractured rock volume using the codas of seismograms from induced microearthquakes, *EOS Trans.*, **72**, 306, 1991.
- Ishida, M. and H. Kanamori, The foreshock activity of the 1971 San Fernando earthquake, California, *Bull. Seism. Soc. Am.*, **68**, 1265-1279, 1978.
- Ito, A., High resolution relative hypocenters of similar earthquakes by cross-spectral analysis method, *J. Phys. Earth*, **33**, 279-294, 1985.
- Ito, A., Earthquake swarm activity revealed from high-resolution relative hypocenters --clustering of microearthquakes, *Tectonophysics*, **175**, 47-66, 1990.
- Johnson, P.A., Cluster analysis of eastern Washington seismicity, M.S. Thesis, University of Washington, 1989.
- Johnson, P.A. and J.E. Zollweg, The 1986 Darrington, Washington earthquake swarm: evidence for tightly clustered asperities? *EOS Trans. Am. Geophys. Union*, **68**, 46, 1987a.
- Johnson, P.A. and J.E. Zollweg, High-precision relative locations for a northwestern Washington earthquake swarm, *Seis. Res. Lett.*, **58**, 28, 1987b.
- Johnson, P.A. and T.V. McEvilly, Fluids and faulting: Suggestive evidence and crucial tests at Parkfield. *U.S. Geol. Surv. Proc. Workshop LXIII*,

*Open-File Rep.* **94-228**, 1994.

Johnson, P.A. and T.V. McEvilly, Parkfield seismicity: Fluid driven?, *J. Geophys. Res.*, **100**, 12,937-12,950, 1995.

Keck, R.G. and R.J. Withers, A field demonstration of hydraulic fracturing for solids waste injection with real-time passive seismic monitoring, paper SPE 28495, 1994.

Madariaga, R., On the relation between seismic moment and stress drop in the presence of stress and strength heterogeneity, *J. Geophys. Res.*, **84**, 2243-2250, 1979.

Molnar, P., Earthquake recurrence intervals and plate tectonics, *Bull. Seism. Soc. Am.*, **69**, 115-133, 1979.

Motoya, Y., and K. Abe, Waveform similarity among foreshocks and aftershocks of the October 18, 1981 Eniwa, Hokkaido, earthquake, *Earthquake Predict. Res.*, **3**, 627-636, 1985.

Nadeau, R.M., M. Antolik, P. A. Johnson, W. Foxall, and T. V. McEvilly, Seismological studies at Parkfield III: Microearthquake clusters in the study of fault-zone dynamics, *Bull. Seism. Soc. Am.*, **84**, 247-263, 1994.

Nadeau, R.M., W. Foxall, T.V. McEvilly, Clustering and periodic recurrence of microearthquakes on the San Andreas fault at Parkfield, California, *Science*, **267**, 503-507, 1995.

Omori, F., Horizontal pendulum observations of earthquakes in Tokyo: Similarity of the seismic motions originating at neighboring centers, *Publ. Earthquake Invest. Comm. Foreign Lang.*, **21**, 9-102, 1905.

Pearson, C., The relationship between microseismicity and high pore pressures during hydraulic stimulation experiments in low permeability granitic rocks, *J. Geophys. Res.*, **86**, 7855-7864, 1981.

Pechmann, J. C. and H. Kanamori, Waveforms and spectra of preshocks and aftershocks of the 1979 Imperial Valley earthquake, *Bull. Seism. Soc. Am.*, **72**, 237-258, 1982.

Pechmann, J.C. and B.S. Thorbjarnardottir, Waveform analysis of two preshock-main shock-aftershock sequences in Utah, *Bull. Seism. Soc. Am.*, **80**, 519-550, 1990.

- Phillips, W. S, L. S. House, and M. C. Fehler, Vp/Vs and the structure of microearthquake clusters, *Seism. Res. Lett.*, **63**, 56, 1992.
- Phillips, W.S., J.T. Rutledge, T.D. Fairbanks, T.L. Gardner, M.E. Miller and B.K. Schuessler, Reservoir fracture mapping using microearthquakes: Austin chalk, Giddings field, TX and 76 field, Clinton Co., KY, paper SPE 36651, 1996.
- Poupinet, G., W. Ellsworth, and J. Frechet, Monitoring velocity variations in the crust using earthquake doublets: an application to the Calaveras fault, California, *J. Geophys. Res.*, **89**, 5719-5731, 1984.
- Roff, A., W.S. Phillips and D.W. Brown, Joint structures determined by clustering microearthquakes using waveform amplitude ratios, *Int. J. Rock Mech. Geomech. Abs.*, **33**, 627-639, 1996.
- Scotti, O. and F. H. Cornet, In-situ evidence for fluid-induced aseismic slip events along fault zones, *Int. J. Rock Mech. Min. Sci and Geomech. Abstr.*, **31**, 347-358, 1994.
- Spudich, P., and T. Bostwick, Studies of the seismic coda using an earthquake cluster as a deeply buried seismograph array, *J. Geophys. Res.*, **92**, 5719-5731, 1987.
- Stauder, W., and A. Ryall, Spatial distribution and source mechanism of microearthquakes in Central Nevada, *Bull. Seism. Soc. Am.*, **57**, 1317-1345, 1967.
- Sykes, L.R., Earthquake swarms and sea-floor spreading, *J. Geophys. Res.*, **75**, 6598-6611, 1970.
- Warpinski, N.R., T.B. Wright, J.E. Uhl, B.P. Engler, P.M. Drozda, R.E. Peterson and P.T. Branagan, Microseismic monitoring of the B-sand hydraulic fracture experiment at the DOE/GRI Multi-Site project, paper SPE 36450, 1996.



## Figure Captions

- 1) Map (top) and orthogonal cross-section views (bottom) showing borehole station locations for the MHF experiment at Fenton Hill, New Mexico. The reference point is latitude 35.855, longitude -106.6687 and elevation 2652 m above mean sea level. The elevation reference is near ground level. Filled triangles are downhole sensors, open circles mark the injection interval and a gray line represents the injection wellbore (EE-2). Arrows in the map view define view directions for the two cross-section plots.
- 2) Initial locations of microearthquakes induced during the MHF experiment at Fenton Hill: A) Every fourth event shown in map (top) and cross-section (bottom) views, B) All 8000 high-quality locations shown in the cross-section view looking west, along with the boxes used to select cluster events. Wells are shown in the cross sections. Stations EE-1 and EE-3 are shown as triangles. Arrows in the map view define view directions for the two cross-section plots.
- 3) Vertical-component seismograms from events from clusters 1 (top three) and 2 (bottom three) recorded by the EE-1 sensor. The time origin is set at the P-wave arrival.
- 4) Velocity for which slant-stack energy was maximized, independent of propagation direction, versus time from the event origin for cluster-1 events recorded by the EE-1 sensor. A vertical-component seismogram is plotted for reference.
- 5) Map (top) and orthogonal cross-section views (bottom) of cluster hypocenters. Plots depict relocated hypocenters except as noted: a) cluster 1 before relocation, b) cluster 1, c) cluster 2, with dissimilar waveform events circled, d) cluster 3, e) cluster 4, f) cluster 5, g) sub-cluster 5A, and h) sub-cluster 5B. Arrows in the map view define orthogonal view directions for the two cross-section plots. One view direction is chosen along the strike or trend of the hypocenter pattern. In ambiguous cases, the direction arrow marking the strike or trend is identified.
- 6) Equal-area stereo projection of the RMS slant-stack amplitude versus propagation direction leaving the cluster for: a) cluster 1 windows 0.13 s (S wave) and 0.28 s (S coda), and b) cluster 5B windows 0.26 s (S wave), 0.29 s and 0.33 s (S coda). The slant stack velocity was 3.5 km/s. Contours represent 40% (cluster 1 only), 80%, 96% and 99.5% of the RMS stack range. Energy leaving the cluster in an upward direction is shown on the left side, downward on the right. 30° intervals of azimuth and inclination are

indicated. North is to the top of the page. Triangles indicate straight-ray directions between the cluster and station EE-1.

7) Slant stack of cluster-1 seismograms for velocity 3.5 km/s and direction towards station EE-1 (top) and away from EE-1 (bottom) versus time from the origin. Stacked seismograms are shown at the same scale.

8) Maximum RMS slant stack (circles) and maximum RMS slant stack within  $15^\circ$  of the straight-ray direction connecting cluster and station EE-1 (dots) versus time from the S arrival for six clusters. Stack values were normalized by the maximum for each cluster.

9) Lower hemisphere, equal-area stereo plot of normals to cluster planes (filled squares) and orientations of (true) cluster edge vectors (open circles). Normals and edges are labeled with their cluster name. Gray lines mark cluster planes.

10) Lower hemisphere, equal-area stereo plot of normals to planes (filled squares) and orientations of linear features (open circles) from this study (symbols labeled with cluster name), as well as normals to planes identified in the MHF seismicity using the three-point method (filled squares labeled with an F), and normals to planes and linear features found by clustering MHF events by their S-to-P amplitude ratios (no labels).

11) Lower hemisphere, equal-area stereo plots of orientations of principal stress axes (left) and the ratio of shear to effective normal stress on a plane versus the normal to that plane (right) indicating the range of planar orientations where slip may occur. On the right, white represents ratios less than 0.6, gray, between 0.6 and 1.0 and black, greater than 1.0. Also shown are the normals to slip planes identified using various methods from Figure 9 (filled squares). The top stress field best satisfies the slip-plane results:  $\sigma_1$  97 MPa, trend N12°E, plunge 79°;  $\sigma_2$  54 MPa, trend N87°W, plunge 2°; and  $\sigma_3$  43 MPa, trend N178°W, plunge 11°. The middle stress field was determined using pressurization and wellbore breakout data:  $\sigma_1$  95 MPa, plunge 90°;  $\sigma_2$  57.5 MPa, trend N14°E, plunge 0°; and  $\sigma_3$  45 MPa, trend N104°E, plunge 0°. The bottom stress field was calculated using focal mechanisms of large MHF events, then rotated as described in the text:  $\sigma_1$  145 MPa, trend N157°E, plunge 8°;  $\sigma_2$  106 MPa, trend N60°E, plunge 61°; and  $\sigma_3$  48 MPa, trend N109°W, plunge 28°. Pore pressure was set to 40 MPa for all slip calculations.

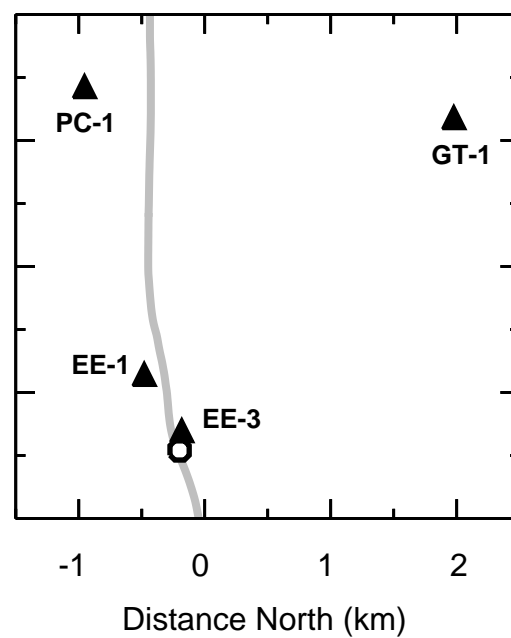
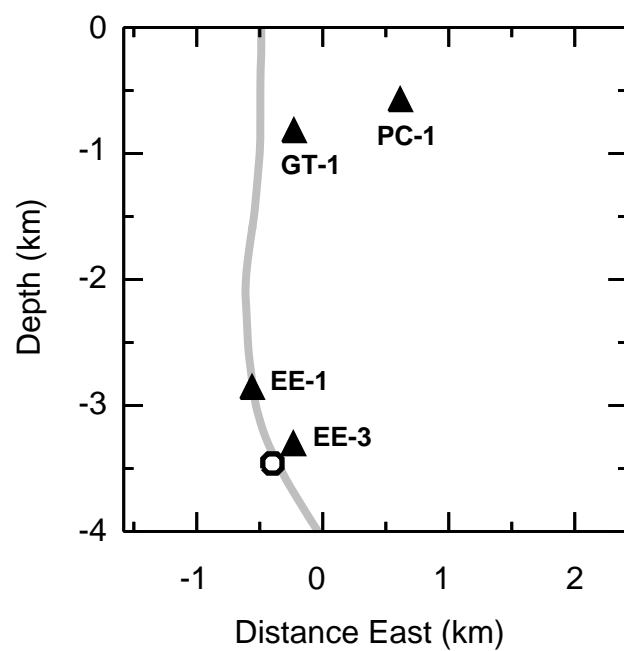
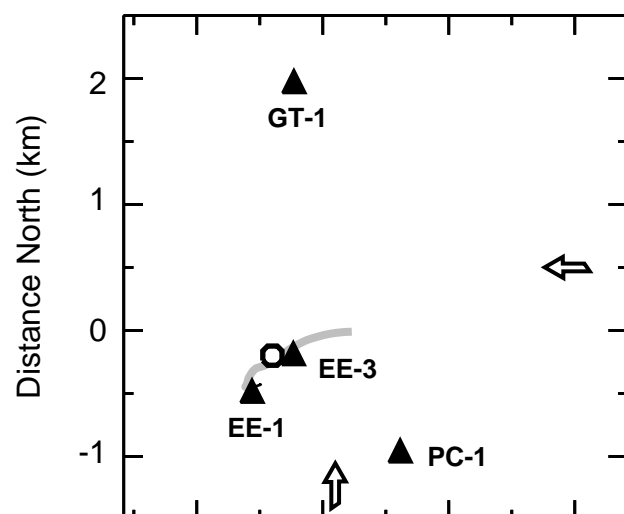


Figure 1

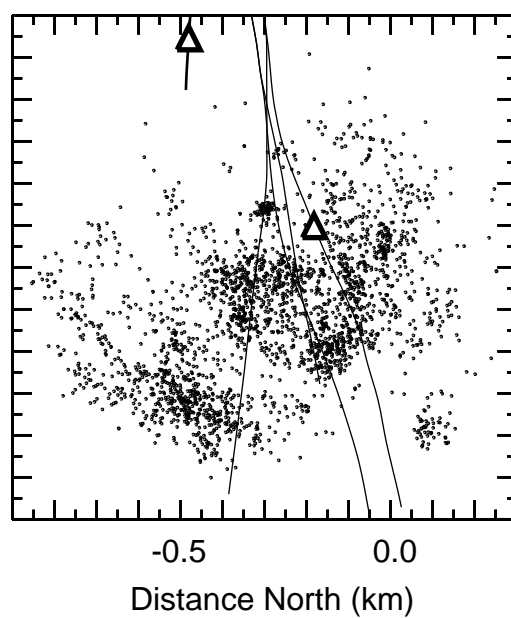
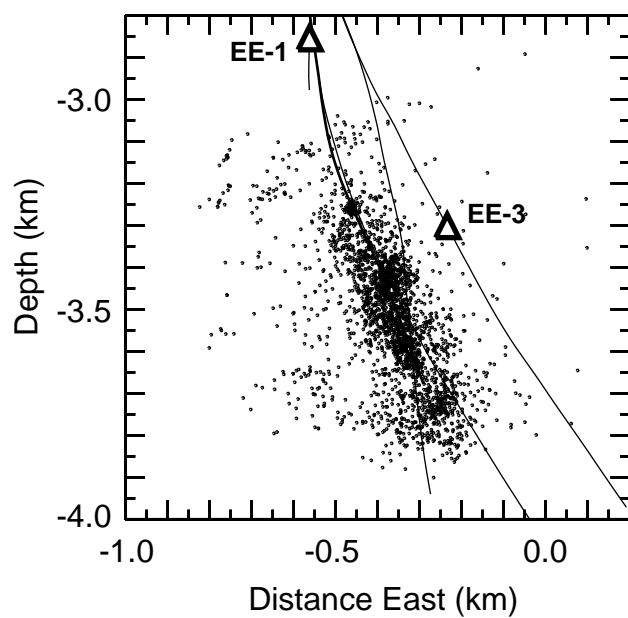
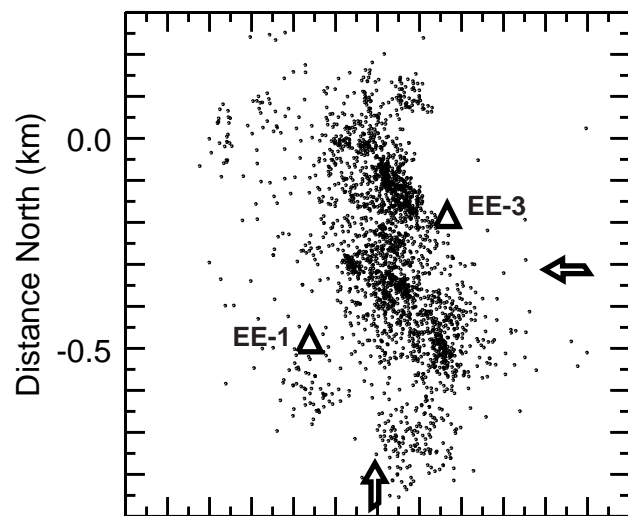


Figure 2A

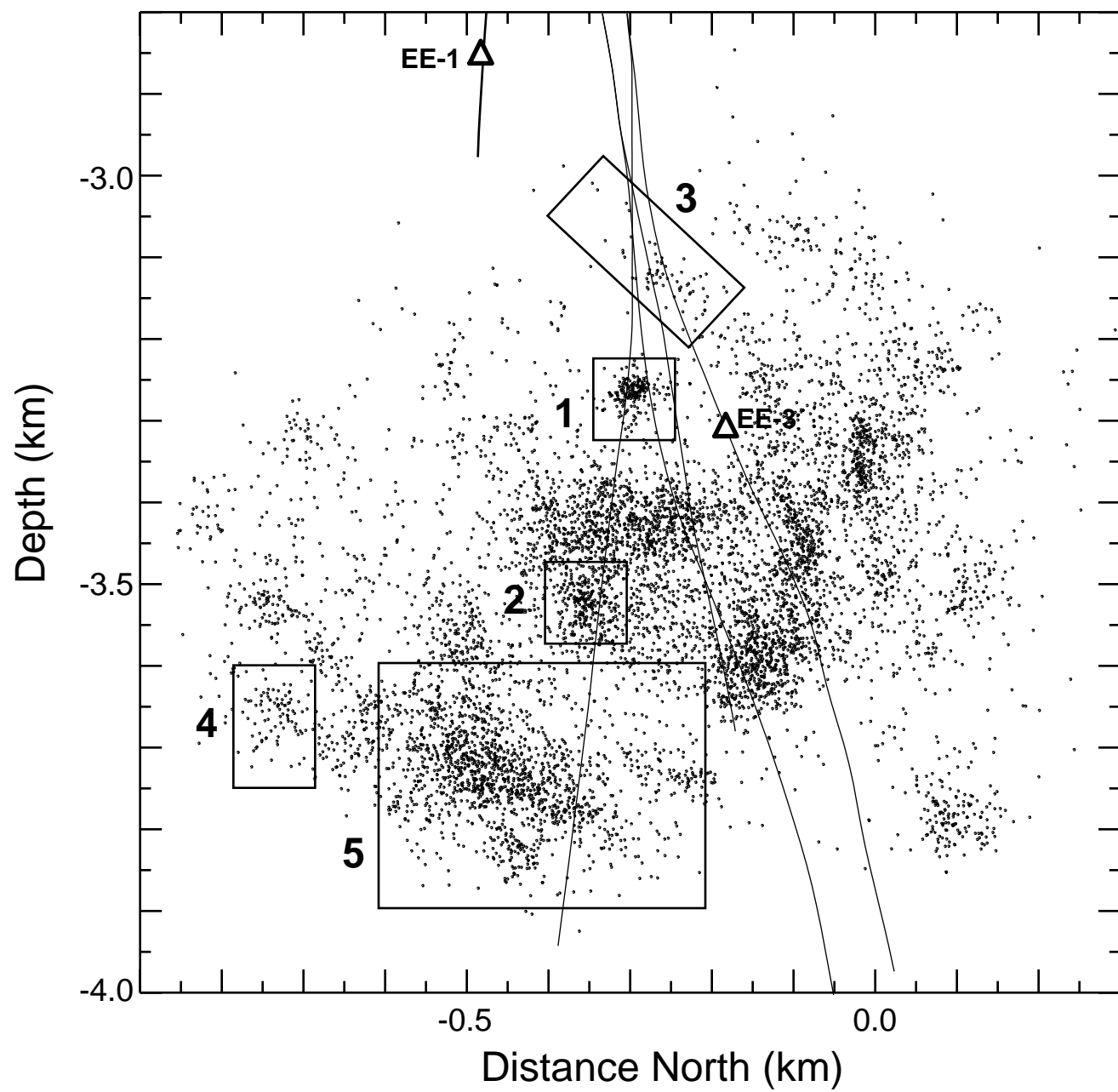


Figure 2B

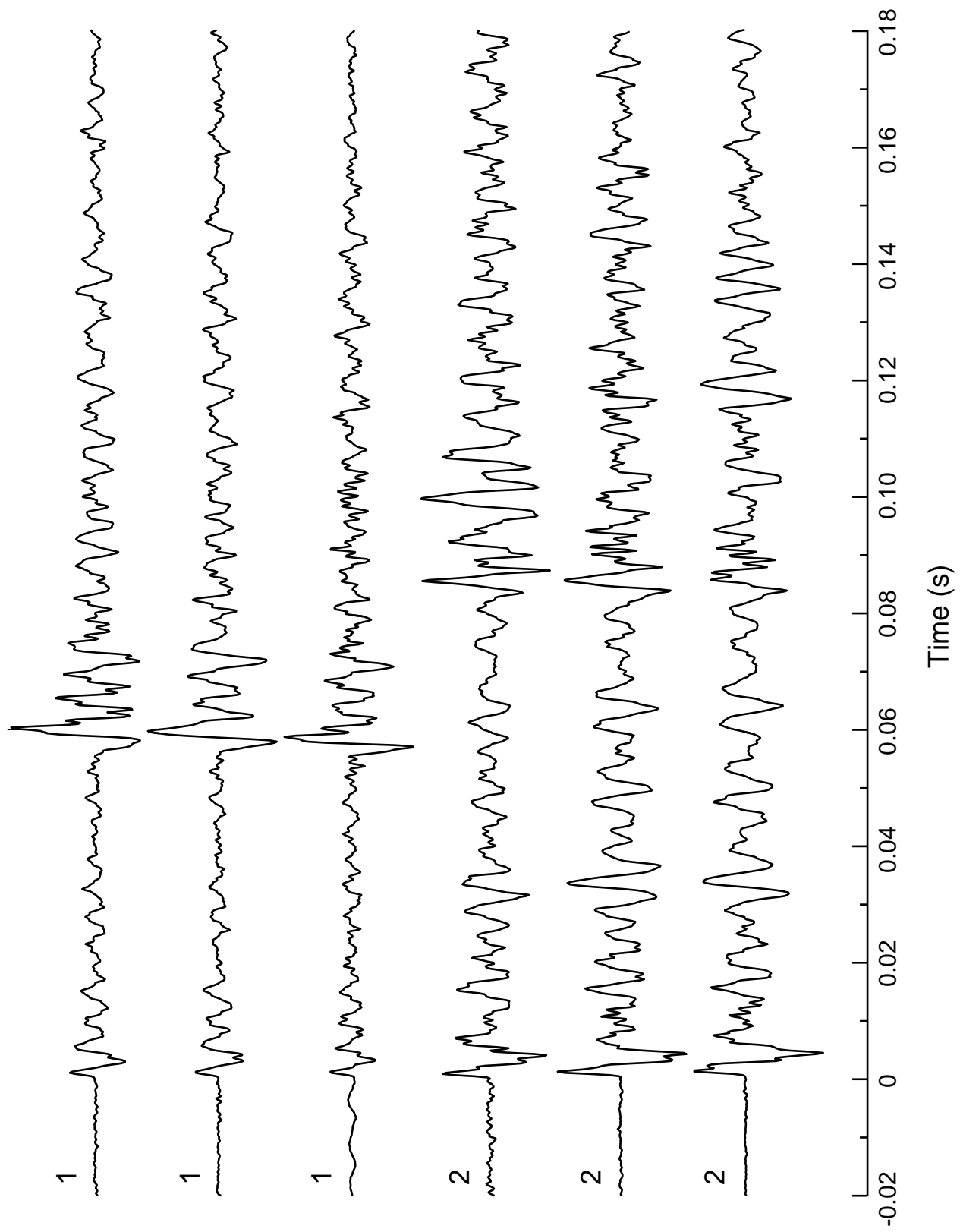


Figure 3

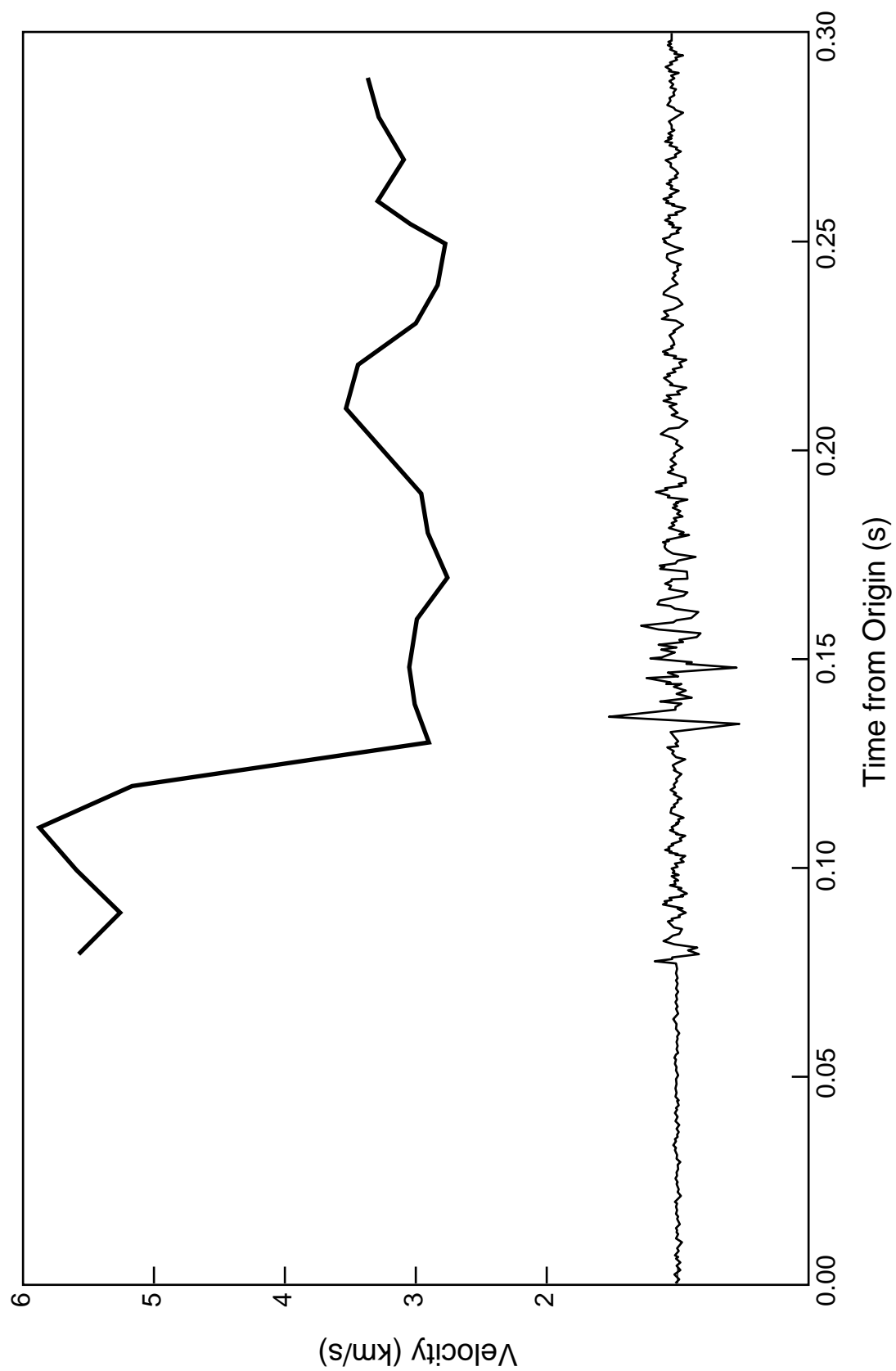


Figure 4

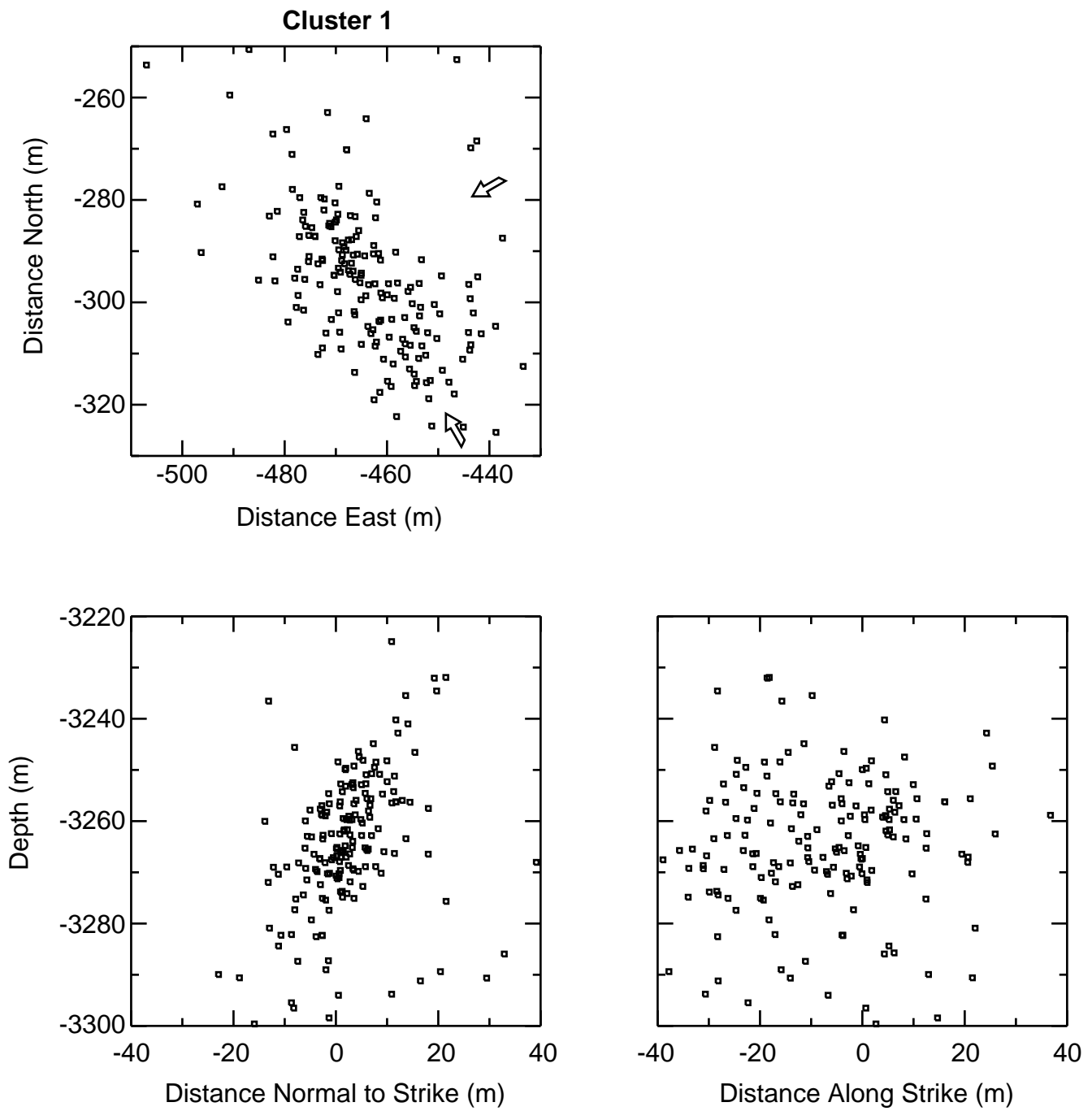


Figure 5a



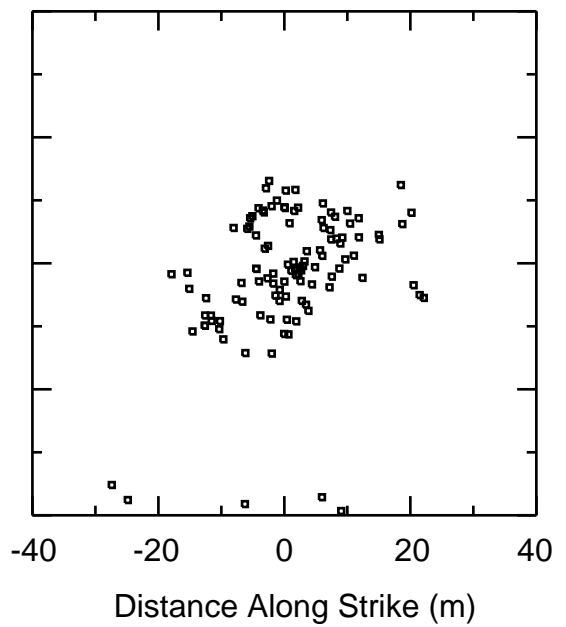
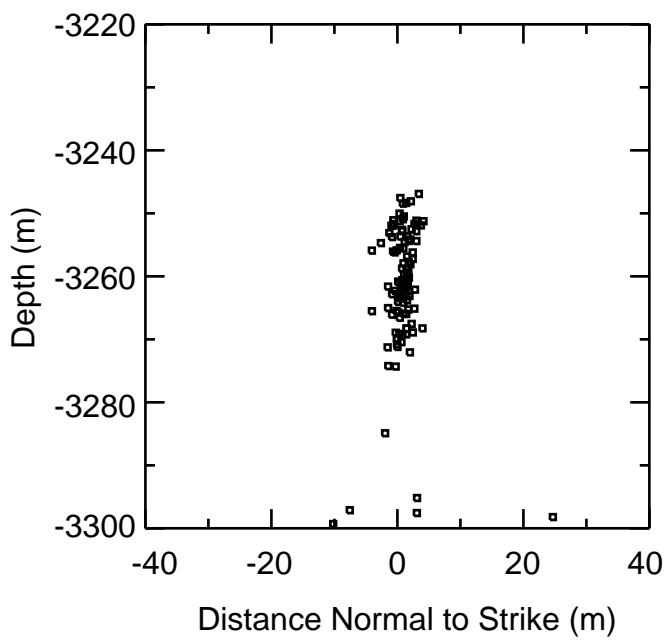
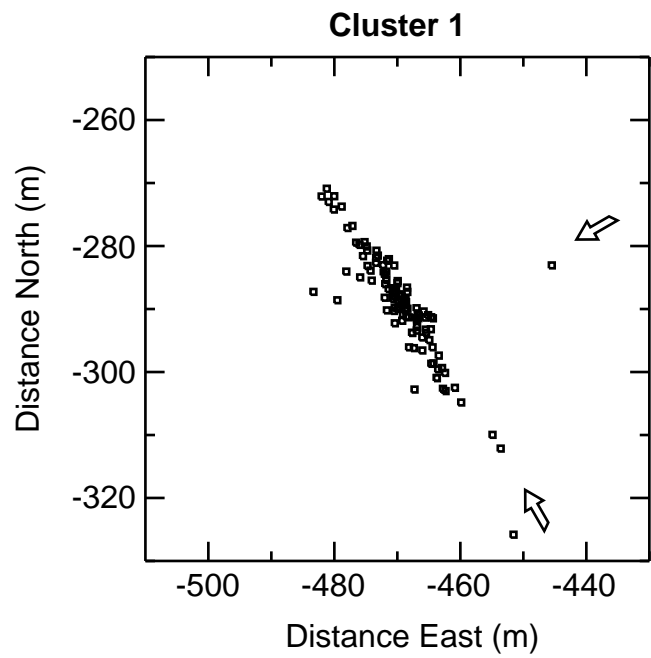


Figure 5b

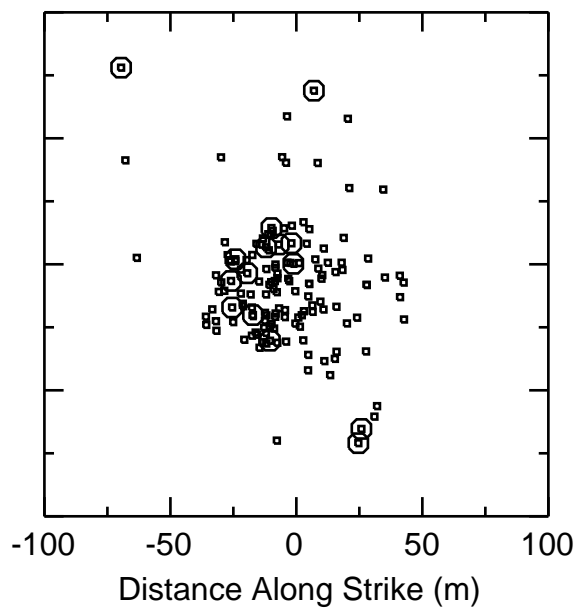
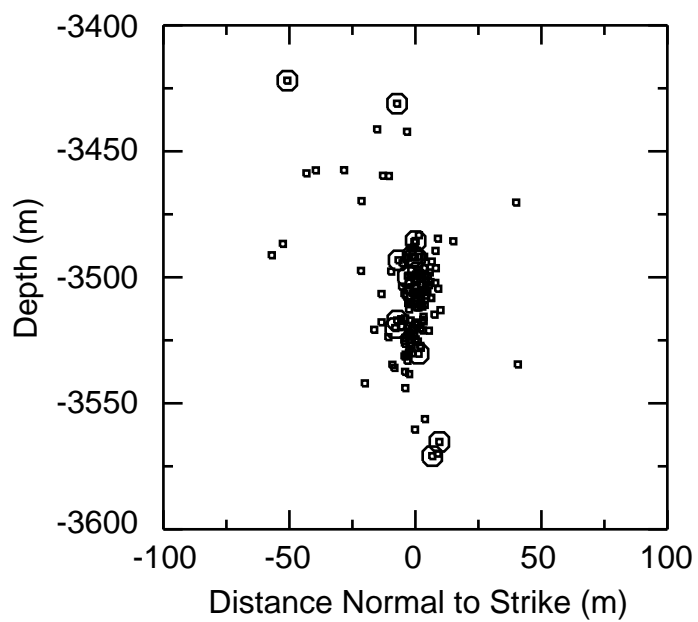
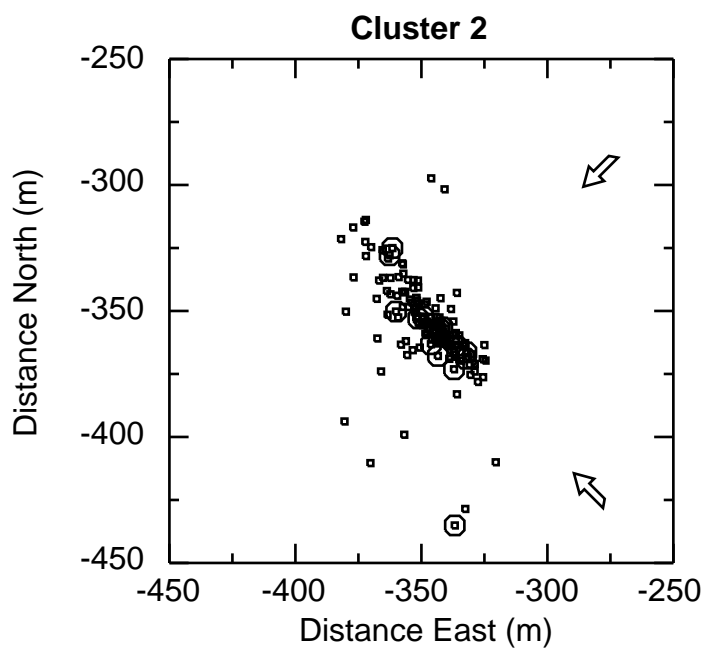


Figure 5c

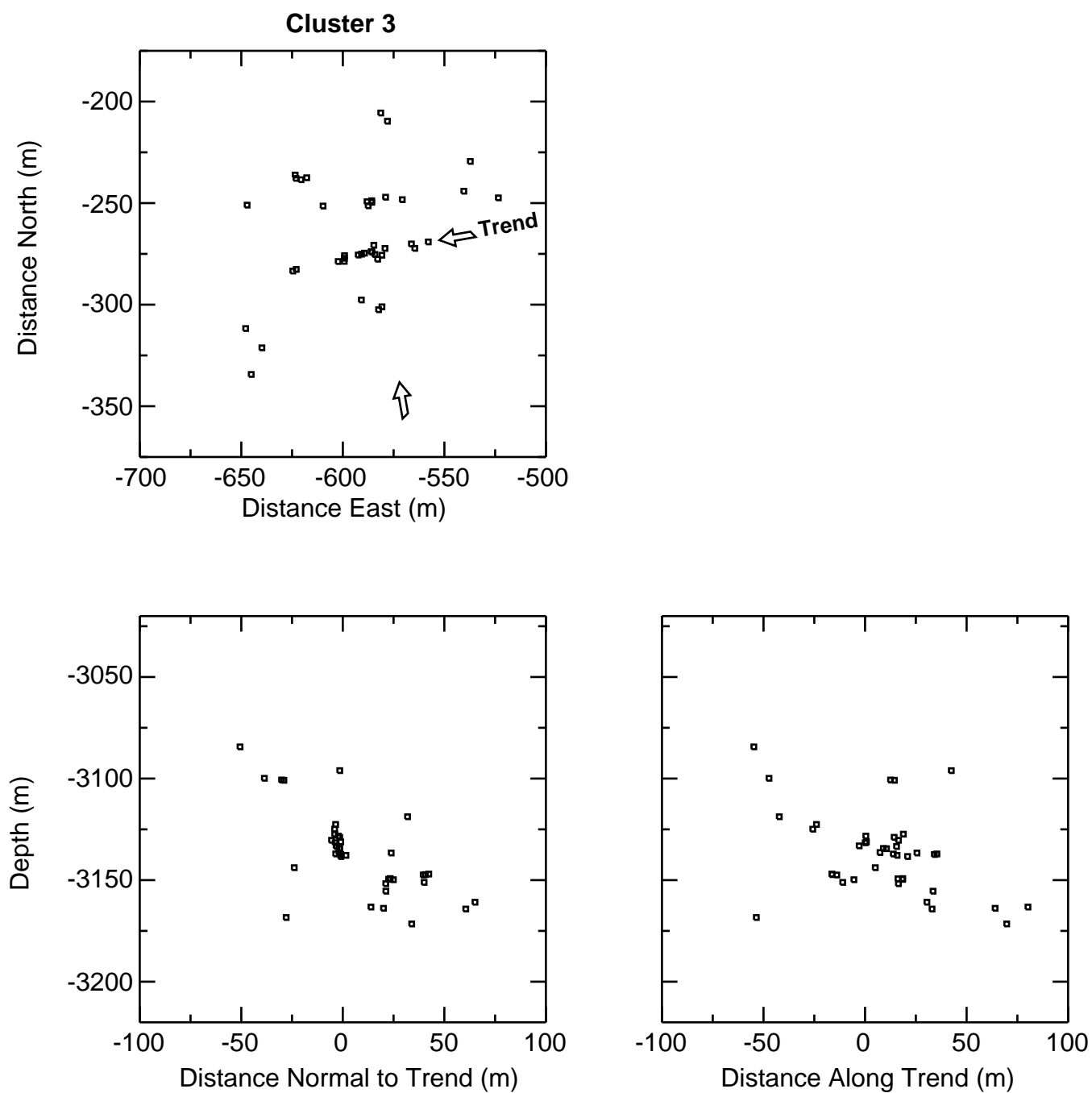


Figure 5d

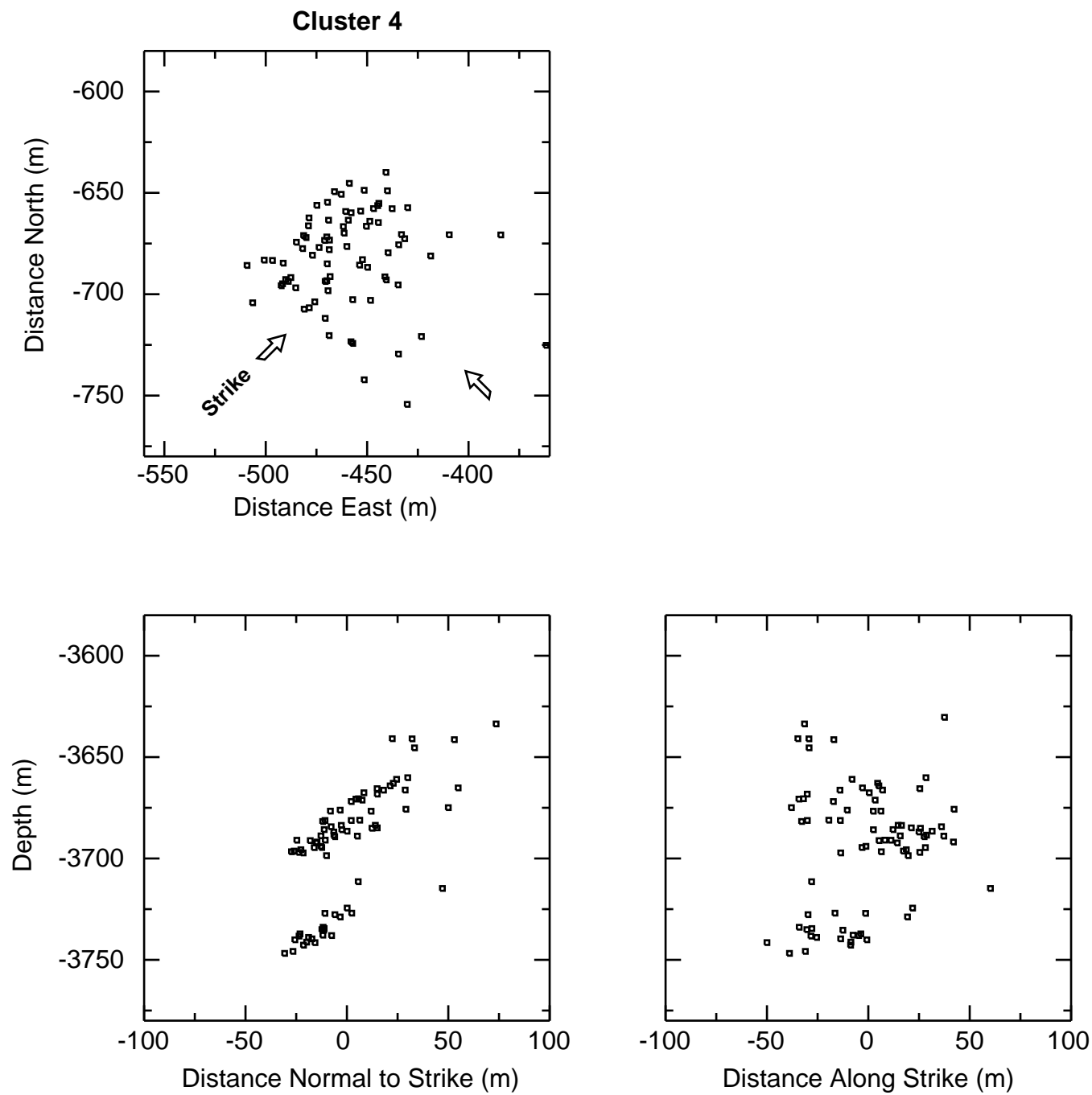


Figure 5e

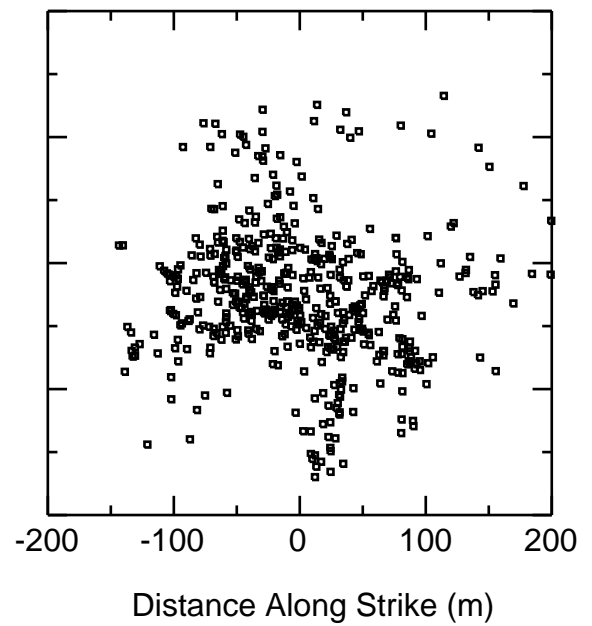
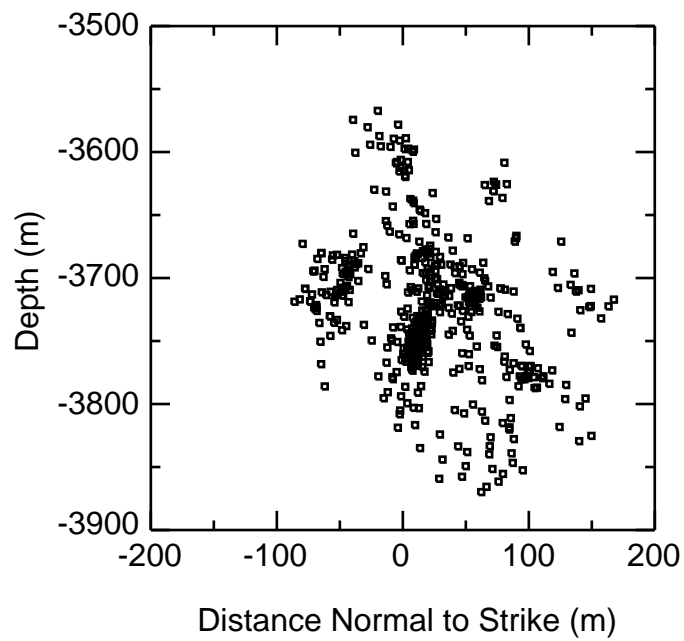
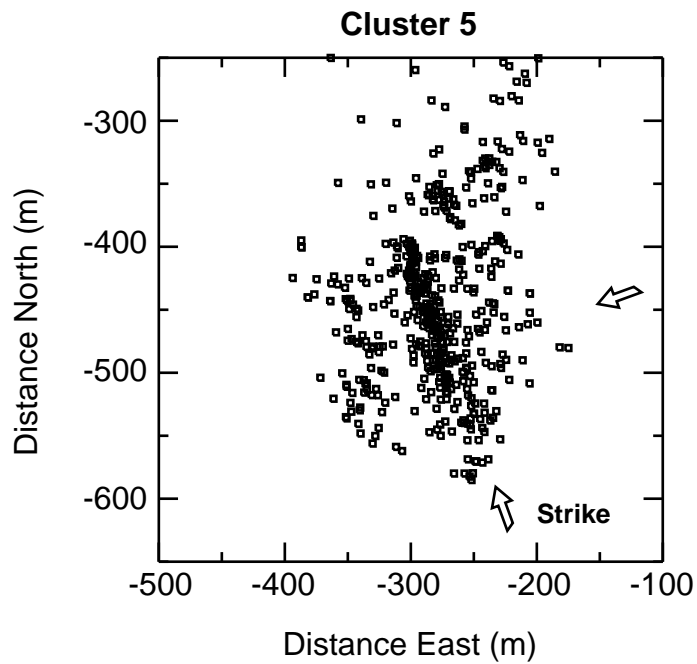


Figure 5f

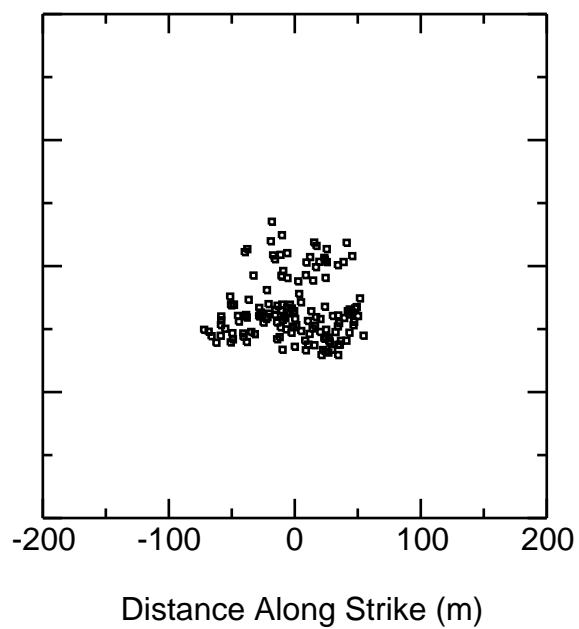
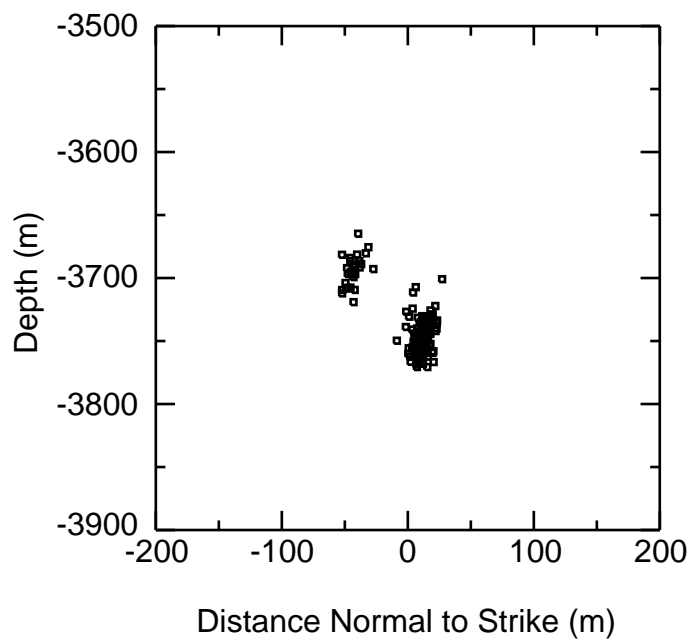
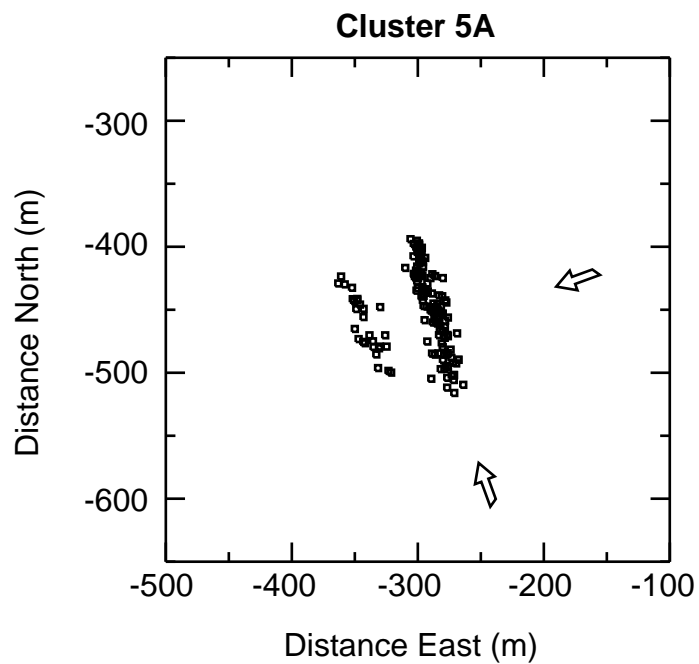


Figure 5g

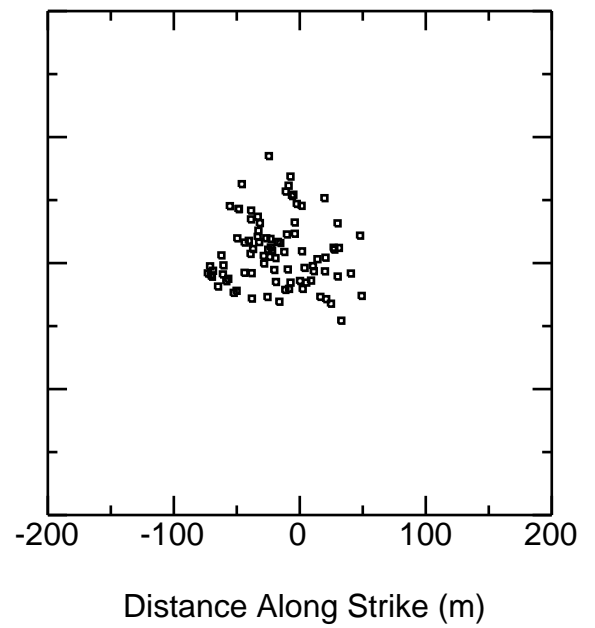
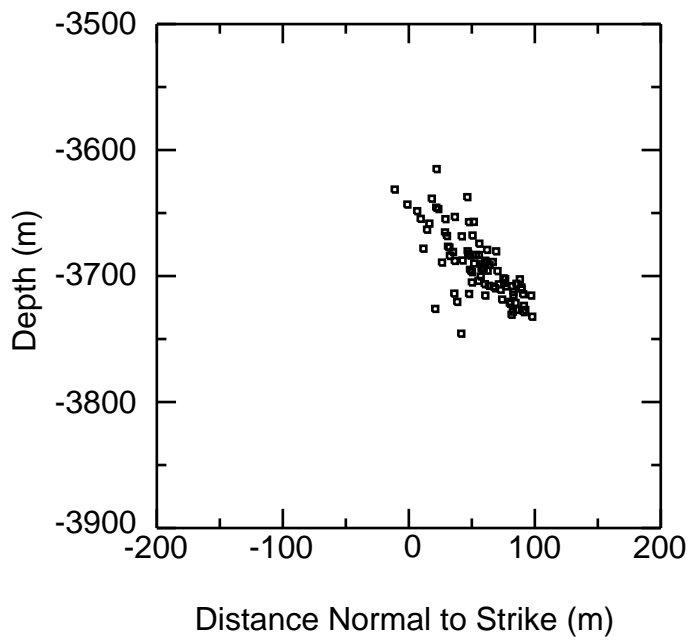
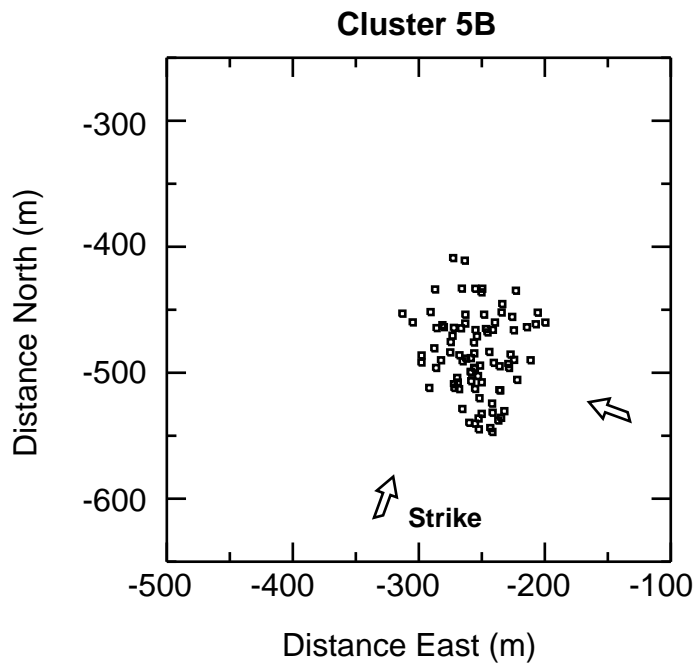


Figure 5h

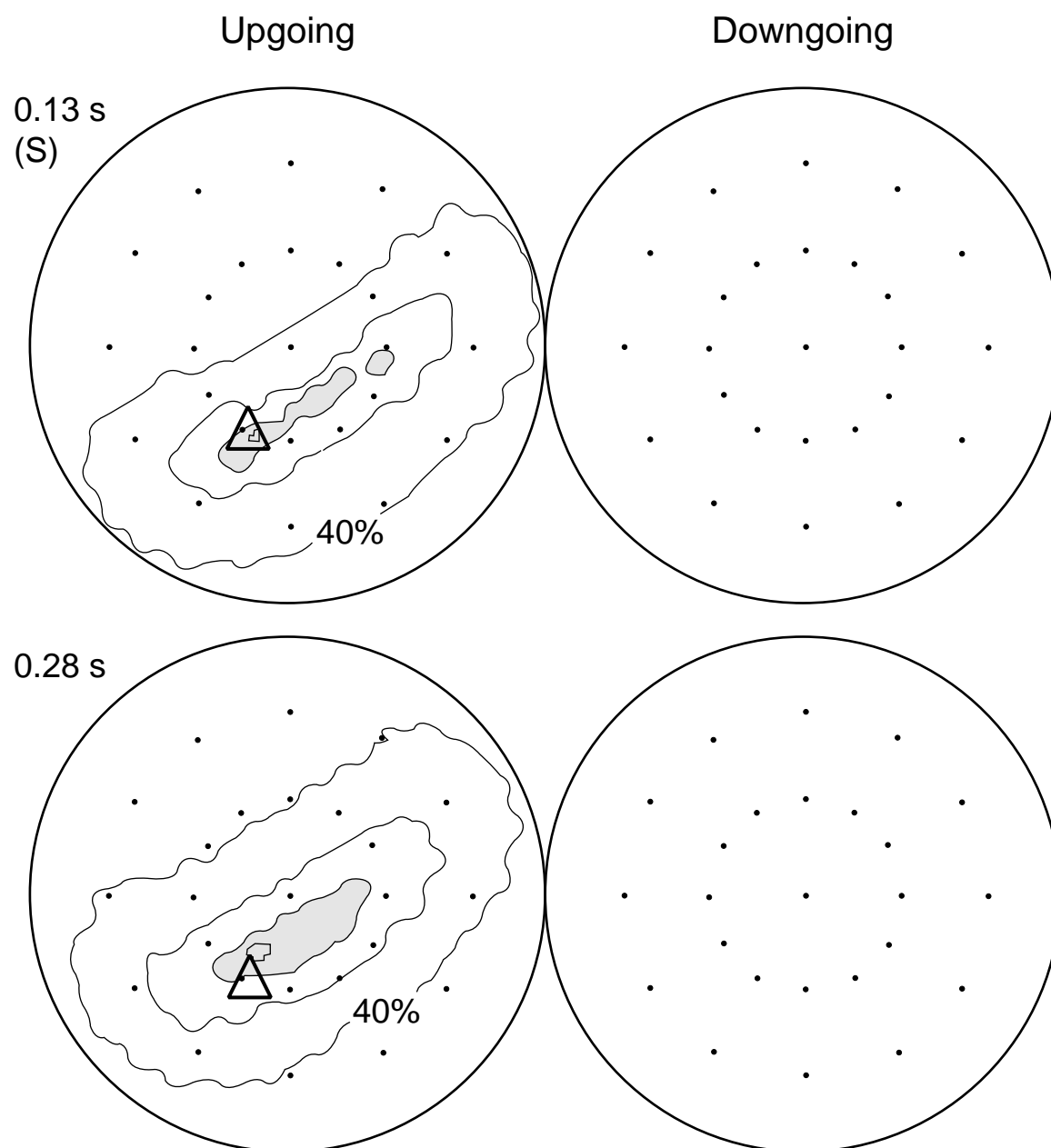


Figure 6a



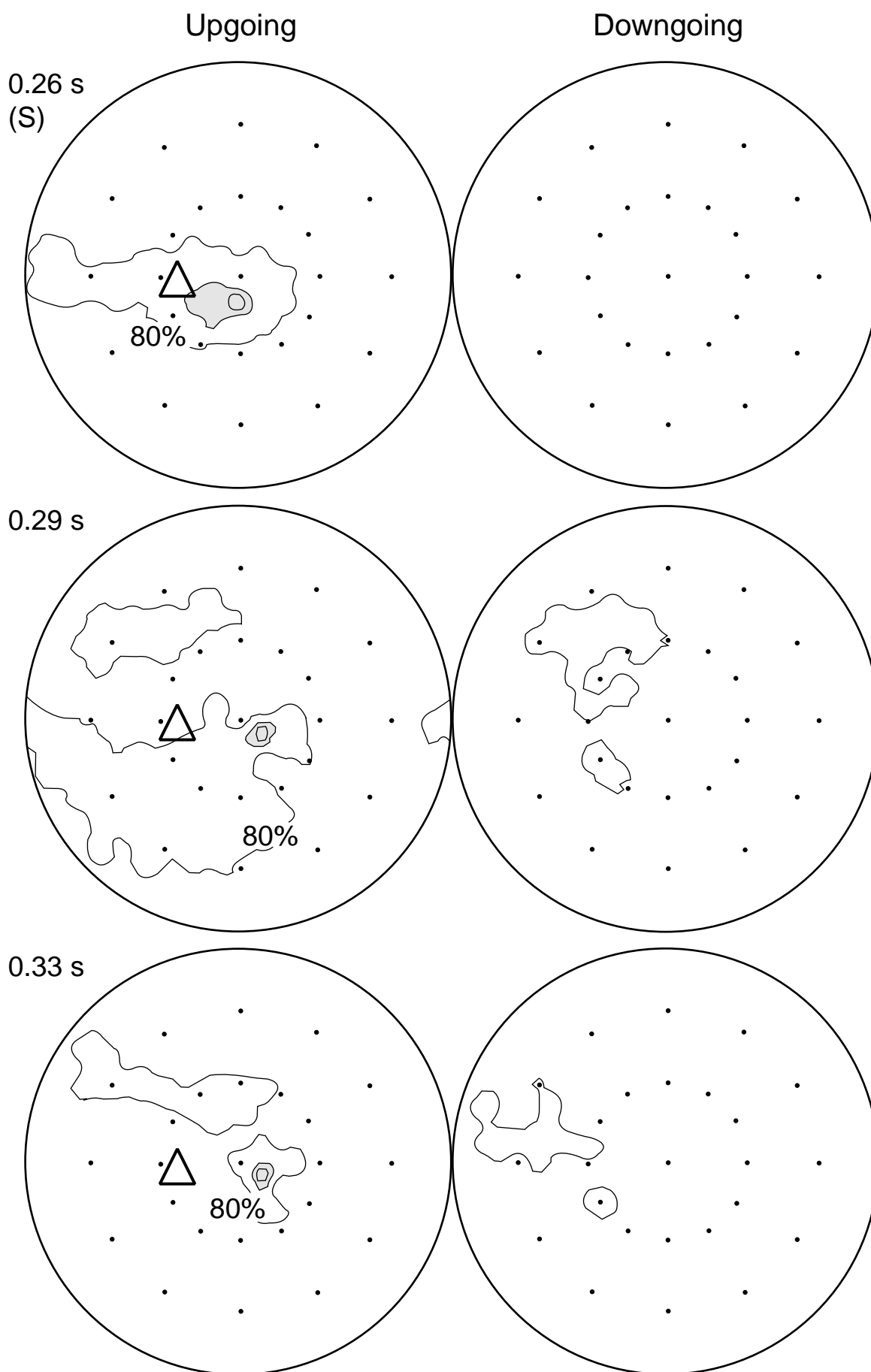


Figure 6b

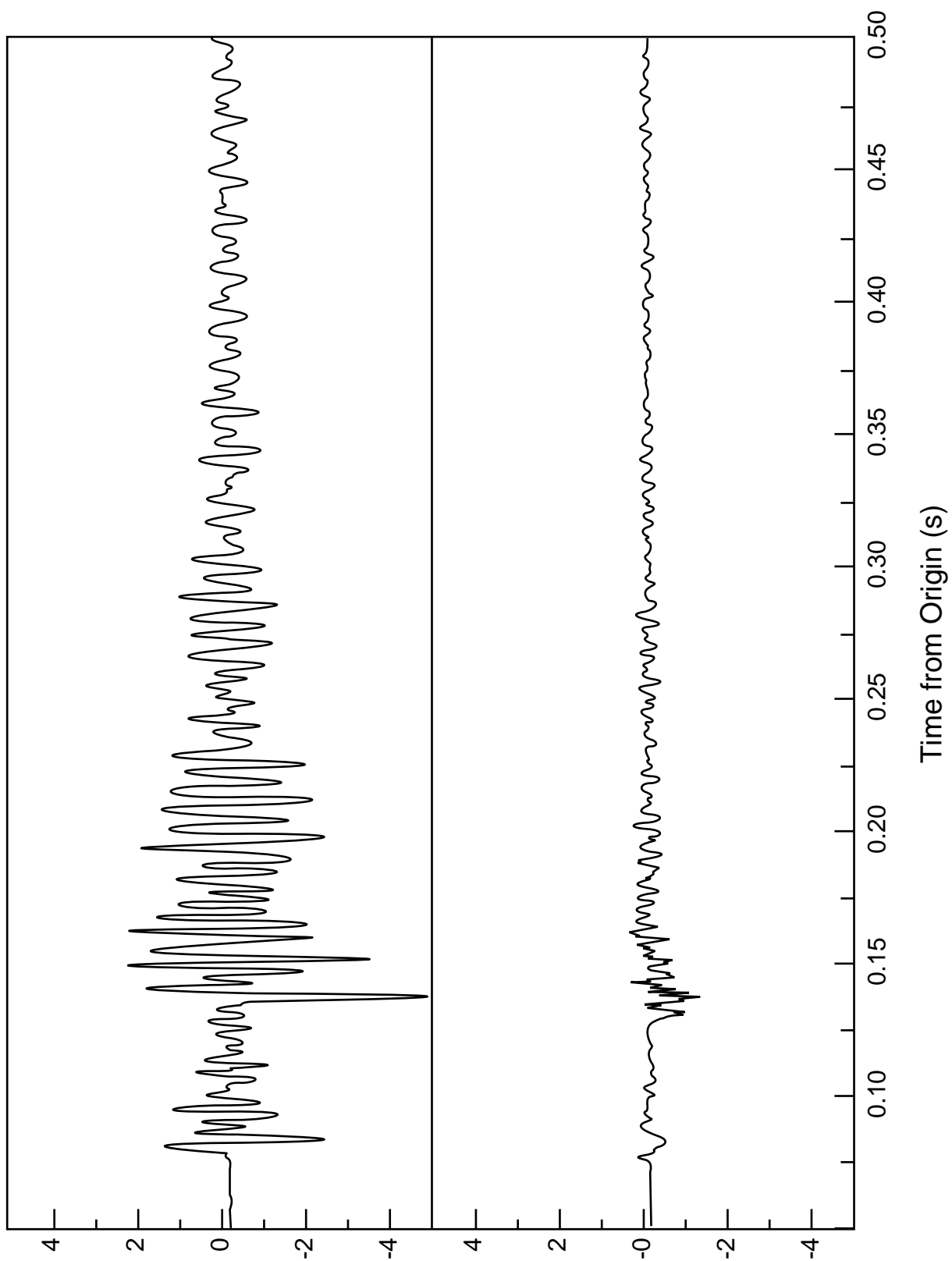


Figure 7

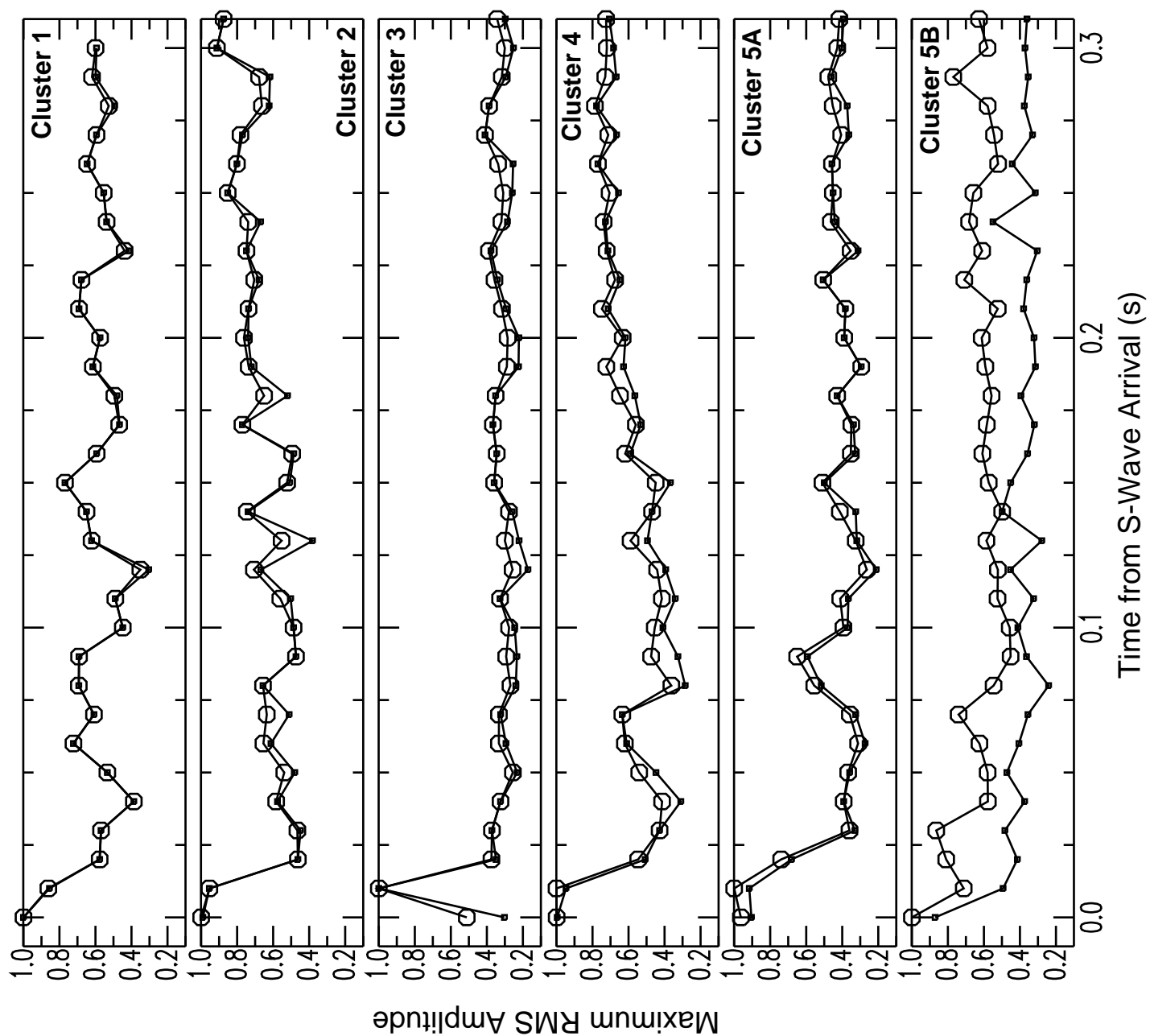


Figure 8

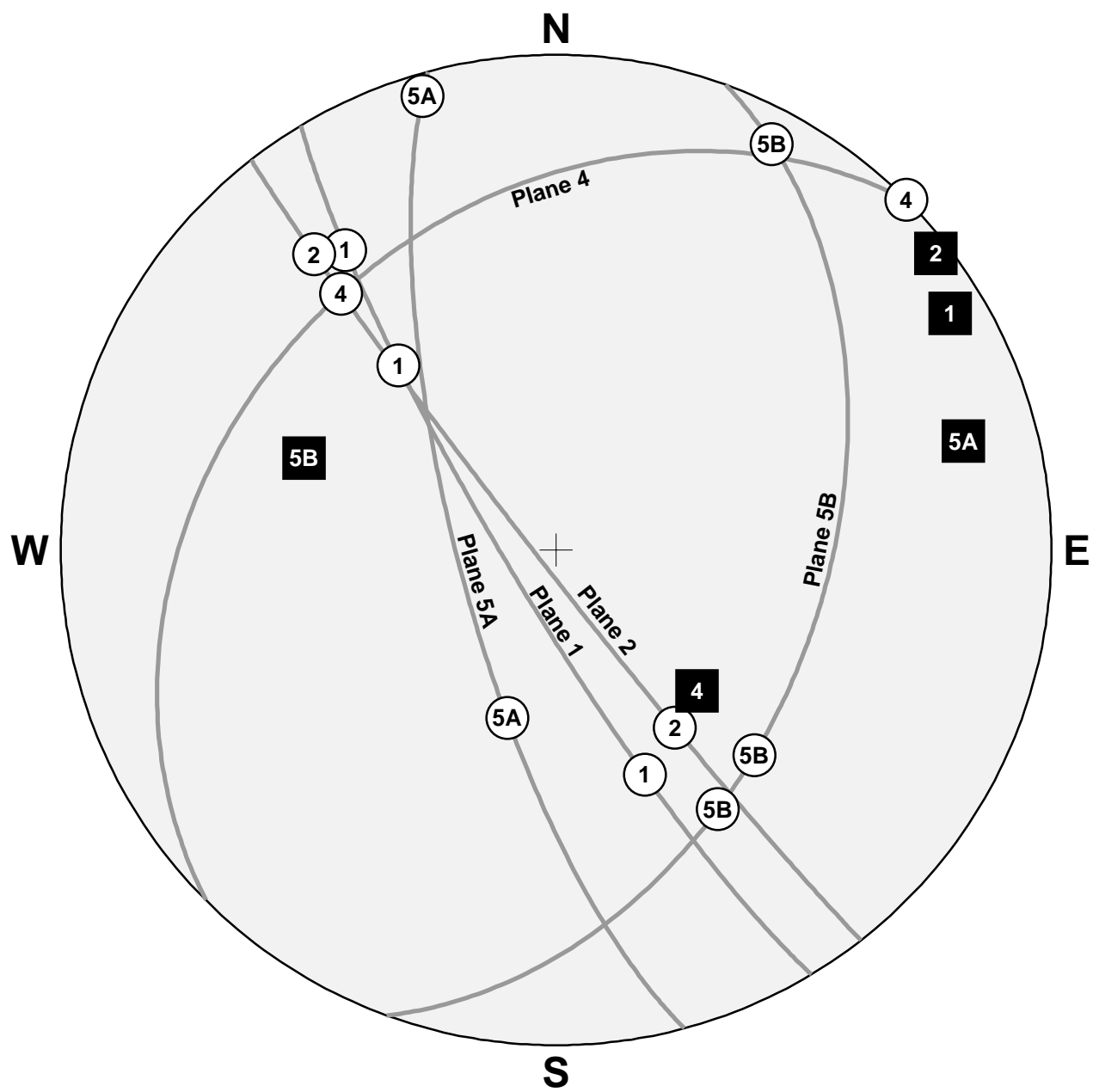


Figure 9

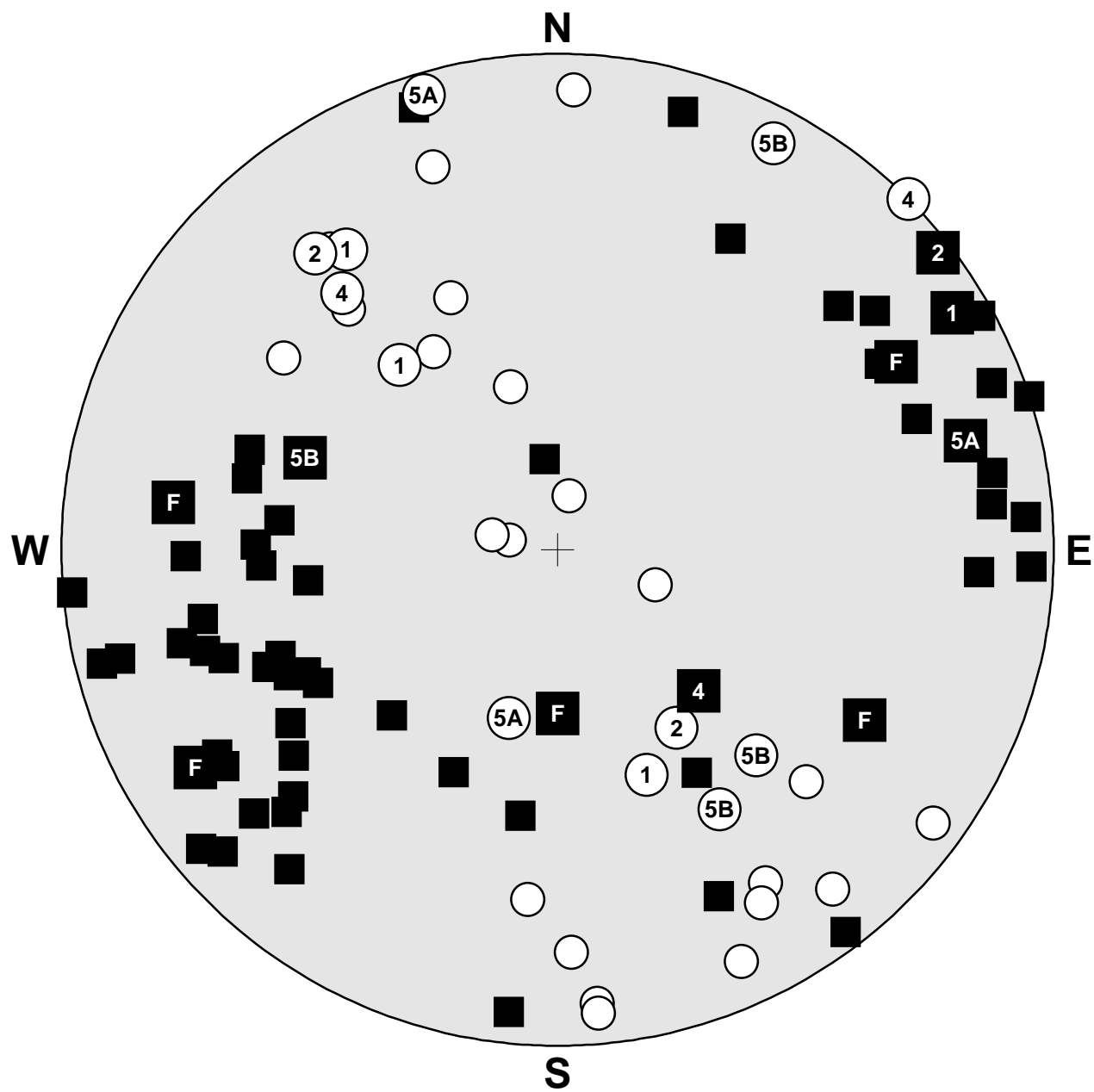


Figure 10

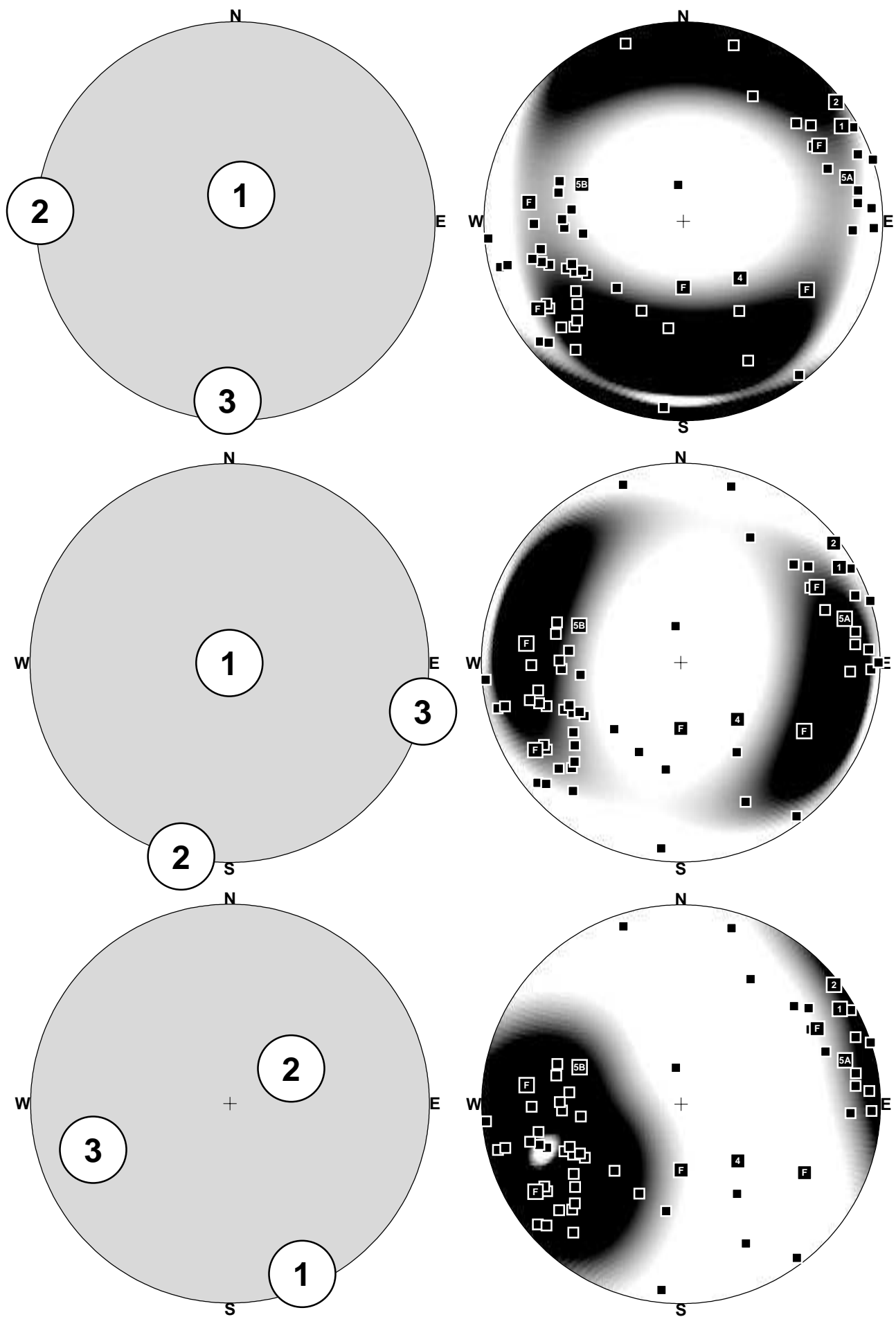


Figure 11

Table 1  
Standard Deviation of Arrival Time Residuals

Cluster	Original Locations (ms)	New Locations (ms)
1	0.2	0.1
2	1.8	0.9
3	0.5	0.4
4	2.2	0.9
5 A	1.8	1.1
5B	1.8	1.1

Table 2  
Best Fit Principal Axes of 90% Confidence Ellipsoids

Cluster	Major Axis			Intermediate Axis			Minor Axis			Misfit
	Magnitude	Trend	Plunge	Magnitude	Trend	Plunge	Magnitude	Trend	Plunge	
	(m)			(m)			(m)			
1	6	-75°	39°	1.5	170°	27°	0.8	55°	39°	2°
2	21	142°	69°	16	-75°	17°	9	19°	12°	17°
3	16	-86°	30°	4	170°	22°	2	50°	51°	2°
4	28	-91°	19°	16	142°	61°	11	7°	22°	11°
5A	22	-91°	47°	20	94°	43°	13	2°	2°	20°
5B	21	-111°	73°	19	91°	15°	12	-1°	6°	18°

Trend is measured clockwise from north, plunge down from horizontal.

Misfit is the average absolute value of the angular residuals.